



Light-induced static magnetization: Nonlinear Edelstein effectHaowei Xu,¹ Jian Zhou ,¹ Hua Wang,¹ and Ju Li ^{1,2,*}¹*Department of Nuclear Science and Engineering, Massachusetts Institute of Technology, Cambridge, Massachusetts 02139, USA*²*Department of Materials Science and Engineering, Massachusetts Institute of Technology, Cambridge, Massachusetts 02139, USA*

(Received 19 October 2020; revised 17 April 2021; accepted 19 April 2021; published 13 May 2021)

Light can interact with magnetism in materials. Motivated by the Edelstein effect, whereby a static electric field can generate magnetization in metals, in this work we theoretically and computationally demonstrate that static magnetization can also be generated through light in semiconductors. Such an effect is essentially a second-order nonlinear response and can be considered as a generalization of the Edelstein effect. This nonlinear Edelstein effect (NLEE) applies to semiconductors under both linearly and circularly polarized light, and there are no constraints from either spatial inversion or time-reversal symmetry. With *ab initio* calculations, we reveal several prominent features of NLEE. We find that the light-induced orbital magnetizations can be significantly greater than the spin magnetizations, in contrast to standard intrinsic magnetism where the orbital magnetic moment is strongly quenched under crystal field. We show that in multilayer (multisublattice) materials, different ferromagnetic and ferrimagnetic structures can be realized under photon pumping, depending on the interlayer (intersublattice) symmetry. It is also possible to switch the magnetic ordering in antiferromagnetic materials. The relationship between NLEE and other magneto-optic effects, including the inverse Faraday effect and inverse Cotton-Mouton effect, is also discussed.

DOI: [10.1103/PhysRevB.103.205417](https://doi.org/10.1103/PhysRevB.103.205417)**I. INTRODUCTION**

The generation and manipulation of magnetization is the basis of magnetic information storage and spintronics [1,2]. Conventionally, one uses an external magnetic field to read and write magnetism. However, since the magnetic coupling is weak, a strong magnetic field is usually necessary. For example, recent experimental works show that ~ 1 T magnetic field is required to flip the CrI₃ bilayer from antiferromagnetic into ferromagnetic ordering [3]. Furthermore, in contrast to electric fields or light beams, it is hard to spatially confine and focus the magnetic fields. Modern spintronics requires fast and precise control of magnetization, and one may have to resort to electrical or optical approaches. Physically, it has been demonstrated that an optical or electric field with moderate strength could induce sufficient effective magnetic field and control the magnetism in both bulk materials and thin films efficiently [4–7].

Maxwell's equations in vacuum couple electric field with magnetic field in a standard way, but it would be desirable to further couple magnetization with electric fields by interacting with materials. Indeed, a static electric field can generate and manipulate magnetization. A typical example is the linear Edelstein effect (LEE). LEE is essentially a conversion between electric field and magnetization: In a noncentrosymmetric metal, a static magnetization M can be generated when a static electric field E is applied, and one has $M^i = \zeta_a^i E^a$, where ζ_a^i is the response function, while i and a indicate the magnetization and the electric field directions, respectively.

LEE was first theoretically proposed [8] and then experimentally realized [9,10]. Recently, there has been growing interest in LEE [5,11–13], and it was suggested that LEE can potentially switch the magnetic orderings of magnetic materials [5,13]. However, LEE only exists in metallic systems, and the electric field also generates a charge current (Ohm current). As a result, sometimes the Edelstein effect is also described as the conversion between charge current and magnetization. As we will elaborate later, the Edelstein effect and Ohm current have a similar physical origin and can be regarded as cousin processes. Another effect that can convert an electric field to magnetization is the magnetoelectric effect [14], which can also be described by $M^i = \alpha_a^i E^a$. The magnetoelectric effect works in insulating materials, but it requires the breaking of both time-reversal and spatial inversion symmetry. In the following we focus more on nonmagnetic materials, i.e., with time-reversal symmetry, at the ground state.

Besides a static electric field, we will show how light can be used to manipulate magnetization. As electromagnetic waves, light has alternating electric and magnetic field components, both of which can interact with magnetization. The first observation of the interaction between light and magnetism (magneto-optical effect) dated back to the 1840s, when Faraday experimentally discovered that the polarization plane of a linearly polarized light would be rotated when light propagates in magnetic materials. This phenomenon, dubbed the Faraday effect (and a related magneto-optic Kerr effect in reflection mode), vividly demonstrates that magnetism has an influence on light, and then finds wide applications, such as the measurement of magnetism. In recent years, as lasers with high intensity become available, the inverse effects start to attract great attention, which may have applications in ultrafast

*Corresponding author: liju@mit.edu

spintronics and data storage, etc. The magnetic field component can directly interact with magnetic moments through Zeeman coupling [15]. However, the Zeeman coupling is usually weak, so of greater interest is the coupling between the electric field component with magnetization. For example, Ref. [16] made use of the inverse Faraday effect (IFE) and showed that a circularly polarized light (CPL) can generate an effective magnetic field, which can nonthermally manipulate the magnetization of magnetic materials. Later, it was shown [17] that even a linearly polarized light (LPL) can cause coherent spin excitations through the inverse Cotton-Mouton effect (ICME). The optical controls over magnetism are being extensively studied these days [4,7]. In this work, we develop a computational approach to this problem.

The LEE is a first-order response to the electric field ($\delta M \propto E$). In this work, we generalize LEE into the second-order nonlinear Edelstein effect (NLEE). For NLEE, a static magnetization $\delta M \propto E(\omega)E(-\omega)$ is generated under light. $E(\omega)$ is the Fourier component of the oscillating electric field of the light at angular frequency ω . Just as LEE and Ohm currents are cousins, NLEE is the cousin process of the bulk photovoltaic effect [18–20], via which a static charge current is generated under light. We find that the NLEE can induce a larger effective magnetic field than that of LEE at moderate electric field strength ($E \gtrsim 10$ MV/m). The strength of the magnetization generated by NLEE depends linearly on the light intensity, and can be detected by quantum sensors [21] such as SQUID, NV centers, etc., even if the light intensity is mild so that the magnetization generated is too small to be detected by conventional approaches such as magneto-optical Kerr rotation. From symmetry considerations, NLEE is not constrained by either spatial inversion \mathcal{P} or time-reversal \mathcal{T} symmetry, whereas LEE vanishes in \mathcal{P} -conserved systems. In addition, since light can induce electron interband transitions, NLEE can exist in semiconductors and insulators, whereas LEE only exists in metallic systems. Hence, NLEE can be active in many more materials compared with LEE. Notably, magnetization can be generated under LPL in nonmagnetic materials. This is somewhat counterintuitive, as magnetization requires \mathcal{T} breaking while LPL cannot break \mathcal{T} . We attribute this effect to the breaking of \mathcal{T} by energy dissipation due to interband transitions. Furthermore, as an optical effect, NLEE enjoys many salient merits of optical approaches, as it can be noncontact, noninvasive, and ultrafast. These factors render NLEE a potentially effective method for generating and manipulating magnetic structures, including ferro-, ferri-, and antiferromagnetism.

In the following, we first introduce the physical mechanism and theory of NLEE. Then to illustrate some prominent properties of NLEE, we perform *ab initio* calculations in different material systems, including nonmagnetic transition metal dichalcogenides (TMDs) and antiferromagnetic CrI₃ bilayers. We incorporate orbital magnetic moments, as well as spin magnetic moments. Remarkably, we find that the orbital contribution can be stronger than the spin contribution, especially in conventionally nonmagnetic systems. This is opposite to the behavior of the spontaneous magnetization of magnetic materials, where the spin contribution usually dominates. In bilayer MoTe₂, NLEE is sensitive to the stacking pattern of the two MoTe₂ layers, and various optomagnetic orderings,

including antiferromagnetic (AFM) and ferromagnetic (FM), are achievable and controllable. Finally, we discuss the possibility of switching the AFM ordering in the CrI₃ bilayer with NLEE, making use of the spatially varying magnetization. The relationship between NLEE and IFE and ICME is also addressed. Specifically, IFE and ICME are incorporated by NLEE, and NLEE also points out the possibility to generate magnetization in nonmagnetic materials under LPL, which is not captured by IFE or ICME.

II. RESULTS

A. Mechanisms and theory

The electron magnetic moment m has both the spin (S) and orbital (L) angular momentum contributions, and one has $m = \mu_B(2S + L)/\hbar$, where μ_B is the Bohr magneton and the factor of 2 for S is the g factor of the electron spin. The total magnetization of an electron ensemble is the total magnetic moments of all electrons. For example, in nonmagnetic materials, the magnetic moments of all electrons sum up to zero, and the equilibrium magnetization M_0 is thus zero. However, when the electrons are driven out of equilibrium, the electron distribution function would be changed, and a net magnetization δM may arise. A simple example is, in a system where the magnetic moments of all electrons cancel out, if somehow one electron flips its magnetic moment, then the system would acquire a net magnetization. One can see that for the total magnetization to be nonzero, each electron should have a specific magnetic moment (i.e., spin texture and orbital texture). If the magnetic moments of the electrons are random, then the total magnetization would always be zero, no matter what the distribution function looks like. For the spin part, the spin texture could be created by, e.g., spin-orbit coupling (SOC) or magnetic ordering. For the orbital part, the orbital texture is ubiquitous in multiorbital systems, and a nonzero orbital magnetization generally exists.

Various mechanisms can drive the electrons out of equilibrium, thus changing the magnetic state. For the LEE, it is the electric field E that drives the electrons out of equilibrium. Indeed, electrons would move under the electric field, leading to a change in the distribution function. This effect is schematically illustrated in Fig. 1(a): Region X (Y) of the Brillouin zone will have fewer (more) electrons under E , which tilts the Fermi surface. If electrons in X and Y have different spin/orbital polarizations $m^X \neq m^Y$, then a net magnetization change $\delta M \propto m^Y - m^X$ would arise. One can see that the LEE is an *intraband* process and only electrons near the Fermi level contribute—thus the LEE applies only to metals. LEE has a similar physical origin to the Ohm current. At equilibrium, the velocities of all electrons sum up to zero; thus the net charge current is zero, but the electrons in regions X and Y have different velocity $v^X \neq v^Y$. As a result, when the electric field is applied, the velocities of all electrons do not sum up to zero anymore, and a net charge current $j \propto v^Y - v^X$ would be generated.

We now extend from a static electric field to an optical alternating electric field and generalize the first-order LEE to the second-order NLEE. The magnetization induced by an

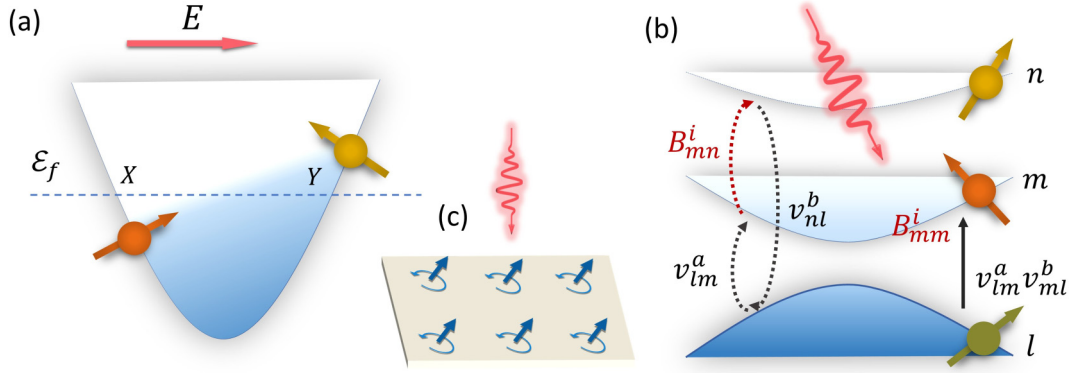


FIG. 1. Simplified physical pictures of (a) linear Edelstein effect and (b) nonlinear Edelstein effect. The blue shading indicates electron occupation. For linear Edelstein effect, the static electric field modifies electron distribution in a single band (intraband process). For nonlinear Edelstein effect, light excites interband transitions between different bands (labeled with l, m, n). The three-band process in Eq. (2) is illustrated by the dashed arrows on the left side of (b), while the two-band process in Eq. (4) is illustrated by the solid arrow on the right side. (c) Local vortices of the photocurrent (blue curved arrows) and the associated orbital magnetization (blue straight arrows) under light (red wavy arrow) illumination.

alternating electric field can be expressed as

$$\delta M^{i,\beta} = \sum_{\Omega=\pm\omega} \chi_{ab}^{i,\beta}(\Omega) E^a(\Omega) E^b(-\Omega). \quad (1)$$

Here a, b , and i indicate the directional component of the electric field and the magnetization, respectively. $E(\omega)$ is the Fourier component of the electric field at angular frequency ω . $\chi_{ab}^{i,\beta}(\omega)$ is the nonlinear response tensor. Superscript β indicates either spin ($\beta = S$) or orbital ($\beta = L$) degree of freedom, and a total ($\beta = T$) magnetic moment is $\delta M^{i,T} = \delta M^{i,S} + \delta M^{i,L}$. Equation (1) suggests that when the ω and $-\omega$ frequency components of the light's electric field are combined, a static magnetization is generated. This is similar to the difference frequency generation and bulk photovoltaic effect. For the difference frequency generation, two photons with frequencies ω_1 and ω_2 are combined, and a third photon with frequency $\omega_1 - \omega_2$ is generated. For the bulk photovoltaic effect, the ω and $-\omega$ frequency components of the electric field are combined, and a displacement of electrons in real space (charge current) is generated. For NLEE, instead of a third photon or an electron displacement, a static magnetic moment is generated. The NLEE magnetization is characterized by the response function $\chi_{ab}^{i,\beta}$, which will be the focus in the following. The formula of $\chi_{ab}^{i,\beta}$ can be obtained from quadratic response theory [18,22–24] (also see Supplemental Material [25] and Refs. [18,22,26–33]). Within the independent particle approximation, it can be expressed as

$$\chi_{ab}^{i,\beta}(\omega) = -\frac{\mu_B e^2 V_{\text{u.c.}}}{\hbar^2 \omega^2} \int \frac{d\mathbf{k}}{(2\pi)^3} \times \sum_{mnl} \frac{f_{lm} v_{lm}^a}{\omega_{ml} - \omega + \frac{i}{\tau}} \left(\frac{\beta_{mn}^i v_{nl}^b}{\omega_{mn} + \frac{i}{\tau}} - \frac{v_{mn}^b \beta_{nl}^i}{\omega_{nl} + \frac{i}{\tau}} \right). \quad (2)$$

We have omitted the \mathbf{k} dependence of the quantities in the integrand. μ_B , e , and \hbar are the Bohr magneton, electron charge, and reduced Planck constant, respectively. Here we multiply unit cell volume ($V_{\text{u.c.}}$), so that $\chi_{ab}^{i,\beta}$ corresponds to

the magnetization in a unit cell, rather than a magnetization density. $f_{lm} \equiv f_l - f_m$ and $\hbar\omega_{lm} \equiv \hbar(\omega_l - \omega_m)$ are the difference between equilibrium occupation number and band energy between bands $|l\rangle$ and $|m\rangle$, respectively. $v_{nl} = \langle n|\hat{\mathbf{v}}|l\rangle$ is the velocity matrix. For the spin and orbital contributions, one can set $\beta_{mn} = 2S_{mn} = 2\langle m|\hat{S}|n\rangle$ and $\beta_{mn} = L_{mn} = \langle m|\hat{L}|n\rangle$, where \hat{S} and \hat{L} are spin and orbital angular momentum operators, respectively. The carrier lifetime τ is assumed to be a constant for all electronic states and is set as 0.2 ps in the following. The dependence of $\chi_{ab}^{i,\beta}$ on τ can be found in the Supplemental Material [25]. We define symmetric real and asymmetric imaginary parts of $\chi_{ab}^{i,\beta}$ as

$$\begin{aligned} \eta_{ab}^{i,\beta} &\equiv \frac{1}{2} \text{Re}\{\chi_{ab}^{i,\beta} + \chi_{ba}^{i,\beta}\}, \\ \xi_{ab}^{i,\beta} &\equiv \frac{1}{2} \text{Im}\{\chi_{ab}^{i,\beta} - \chi_{ba}^{i,\beta}\}. \end{aligned} \quad (3)$$

Note that $\eta_{ab}^{i,\beta}$ and $\xi_{ab}^{i,\beta}$ correspond to the response function under LPL and CPL, respectively.

From Eq. (2) one can see that light can excite (virtual) interband transitions of electrons, as illustrated in Fig. 1(b). The virtual transition between band m and l is mediated by n . At equilibrium, the electron tends to occupy states with the lowest energy, so they should reside on the l th band. Under light illumination, the electron can (virtually) transit to the m th band, which has higher energy. If on a \mathbf{k} point, different bands have different spin/orbital polarization, then a net magnetization change δM^i can be established. Similarly, the (virtual) electron interband transition is also the foundation of difference frequency generation and bulk photovoltaic effect. One could use symmetry analysis to examine the response explicitly. Under spatial inversion \mathcal{P} , axial vectors M, S , and L are even, while polar vectors E and v are odd. From both Eqs. (1) and (2), one can deduce that the NLEE does not require \mathcal{P} breaking. This is in contrast to LEE, difference frequency generation, or the bulk photovoltaic effect, which vanish in \mathcal{P} -conserved systems. It is more intriguing to study the NLEE under time-reversal operation \mathcal{T} . Under \mathcal{T} operation, M, S, L , and v are odd, while E is even. From

Eq. (1) one may deduce that the NLEE should vanish in a \mathcal{T} -conserved system under LPL: $\mathcal{T}M = -M$ and $\mathcal{T}E = E$, leading to $\mathcal{T}\chi = -\chi$; thus χ needs to be zero to preserve time-reversal symmetry. However, Eq. (2) would yield a contrary conclusion: \mathcal{T} does not enforce a zero $\chi_{ab}^{i,\beta}$ (see detailed analysis in the Supplemental Material [25]). Intuitively, LPL induces photocurrent with vorticity as it flows past atoms with chiral neighboring surroundings (crystal field), like an eddy when water flows past rocks in a stream. The vortex currents generally lead to a net magnetization. In \mathcal{P} -broken systems, the vortex currents do not exactly cancel, and lead to a net charge current in the bulk, which is the bulk photovoltaic effect. In \mathcal{P} -conserved systems, the net charge current should vanish in the bulk, but there is still a net current on the surfaces, where \mathcal{P} is naturally broken. The contradiction between Eqs. (1) and (2) can be resolved if one considers the dissipation. Light with above-band-gap frequencies can be absorbed by electron interband transitions and then be dissipated as heat. Such dissipation breaks \mathcal{T} of the light-matter system, according to the second law of thermodynamics. Similar reasonings apply to the Ohm current. Under \mathcal{T} , the charge current is odd ($\mathcal{T}j = -j$), while the electric field is even. But the Ohm current does exist. This is because the Joule heat breaks \mathcal{T} , even if the material possesses \mathcal{T} in equilibrium. Actually, the LEE does not require explicit \mathcal{T} breaking either, and the conversion between charge current and magnetization can happen in nonmagnetic materials. This is also because the Joule heat associated with the charge current breaks \mathcal{T} .

Here we would like to discuss further the role of the carrier lifetime τ . In the hypothetical ‘‘clean limit’’ where no dissipation exists ($\tau \rightarrow \infty$), the NLEE tensor should be zero under LPL in a \mathcal{T} -symmetric system, based on the symmetry analysis in Eq. (1). Technically, this is also manifested in Eq. (2), and the reason is as follows. Under time-reversal \mathcal{T} operation, one has $\mathcal{T}v_{mn}(\mathbf{k}) = -v_{mn}^*(-\mathbf{k})$ and $\mathcal{T}\beta_{mn}(\mathbf{k}) = -\beta_{mn}^*(-\mathbf{k})$, where $*$ indicates the complex conjugate. Thus the numerator, which is $N_{mnl} = v_{mn}v_{nl}\beta_{lm}$, would behave as $\mathcal{T}N_{mnl}(\mathbf{k}) = -N_{mnl}^*(-\mathbf{k})$. After the summation over $\pm\mathbf{k}$, the numerator would be purely imaginary. If $\tau = \infty$ and $\frac{i}{\tau} = 0$, then the denominator would be purely real. Therefore, the whole formula is purely imaginary, and cannot contribute to a static magnetization, which should be a real number. From this point of view, Eqs. (1) and (2) are mathematically equivalent even in the ‘‘clean limit.’’ However, in practice, τ cannot and should not go to infinity. Mathematically, Eq. (2) may experience a divergence problem if one sets $\frac{\hbar}{\tau} = 0$, so a finite \hbar/τ is necessary. Such phenomenon is common in, e.g., quantum field theory, where one adds a small but finite imaginary term in the propagator to avoid the divergence at the singular point. Physically, in interacting systems \hbar/τ has a physical meaning of (effective) self-energy, and τ is the lifetime. The electrons are never free particles in a solid-state system, and their linewidth (\hbar/τ) is always finite. Even if the sample is a perfect crystal, there are still electron-electron interactions, electron-phonon interactions, etc. Besides, the application of Eqs. (2) and (4) in the following requires extra care. One should treat Eqs. (2) and (4) as low-order perturbation theory and should not apply them when the system is strongly out of equilibrium.

In the following, we perform *ab initio* calculations to illustrate NLEE in various two-dimensional (2D) materials that have a large surface area to volume ratio and are easily accessible with optical pumping. We first use monolayer TMDs as an example to show that the orbital contribution to the magnetic moment can be significantly greater than the spin contribution in intrinsic nonmagnetic systems. Then we use bilayer TMDs to show that different magnetic orderings can be obtained under LPL, depending on the interlayer stacking symmetry. Finally, we take 2D AFM material CrI₃ to discuss the possible AFM order manipulation under NLEE. We use 2D materials because they are simpler than three-dimensional (3D) materials and various features of NLEE can be better illustrated. The theory of NLEE applies to 3D materials as well, and can generate a larger total magnetic moment in, e.g., thin films and conventional 3D bulks.

B. Monolayer MoTe₂: Spin and orbital contributions

For the spontaneous magnetization in magnetic materials, the contribution from the orbital angular momentum L is usually weaker than that from the spin angular momentum S . Typically the orbital contribution is less than 10% of the total magnetization $m = \mu_B(2S + L)/\hbar$ [34]. This is due to the orbital quenching by a strong crystal field. On the contrary, for the nonequilibrium magnetization, we will show that the orbital angular momentum could contribute more significantly than the spin angular momentum, due to the chirality of the same strong crystal field.

As an example, we use TMDs (MoTe₂) in the 2H phase, which exhibit many peculiar properties and have been widely studied in recent years. Monolayer 2H TMDs possess mirror symmetries \mathcal{M}_x and \mathcal{M}_z , as indicated by the dashed lines in Figs. 2(a) and 2(b). Notably, \mathcal{M}_z enforces Zeeman type (out of plane) spin/orbital texture. Here we need to examine the constraints on NLEE from mirror symmetries. The polar vector \mathbf{E} satisfies $\mathcal{M}_j E^a = (-1)^{\delta_{ja}} E^a$, where δ_{ja} is the Kronecker delta. That is, the j th component of \mathbf{E} is flipped under \mathcal{M}_j . On the other hand, the spin or orbital angular momentum $\boldsymbol{\beta}$ is an axial vector; thus under \mathcal{M}_j , only the j th component of $\boldsymbol{\beta}$ is *not* flipped, and one has $\mathcal{M}_j \beta^i = -(-1)^{\delta_{ji}} \beta^i$. One can show that in systems with \mathcal{M}_j , the NLEE response $\chi_{ab}^{i,\beta}$ vanishes if $\delta_{ji} + \delta_{ja} + \delta_{jb}$ is an even number. Specific to monolayer MoTe₂, with in-plane electric field (E_x or E_y), the only nonvanishing component of the NLEE tensor is $\chi_{xy}^{z,\beta}$, indicating that the magnetization induced by NLEE is along the out of plane direction. Note that if \mathcal{M}_z is broken (e.g., by an electric field or in a Janus structure), then in-plane magnetization should exist.

Here we focus on CPL responses of monolayer MoTe₂ and plot $\xi_{xy}^{z,\beta}$ [Fig. 2(b)]. A prominent feature is that the orbital part $\xi_{xy}^{z,L}$ is about 25 times greater than the spin part $\xi_{xy}^{z,S}$. In other words, under CPL, the NLEE magnetization comes mostly from the orbital contribution, which is opposite to the behavior of equilibrium magnetization M_0 in magnetic materials, where $M_0^L \gg M_0^S$. This phenomenon can be better understood when we assume a sufficiently long relaxation time (\hbar/τ much smaller than the band gap of the material) and use the two-band approximation; then we can simplify

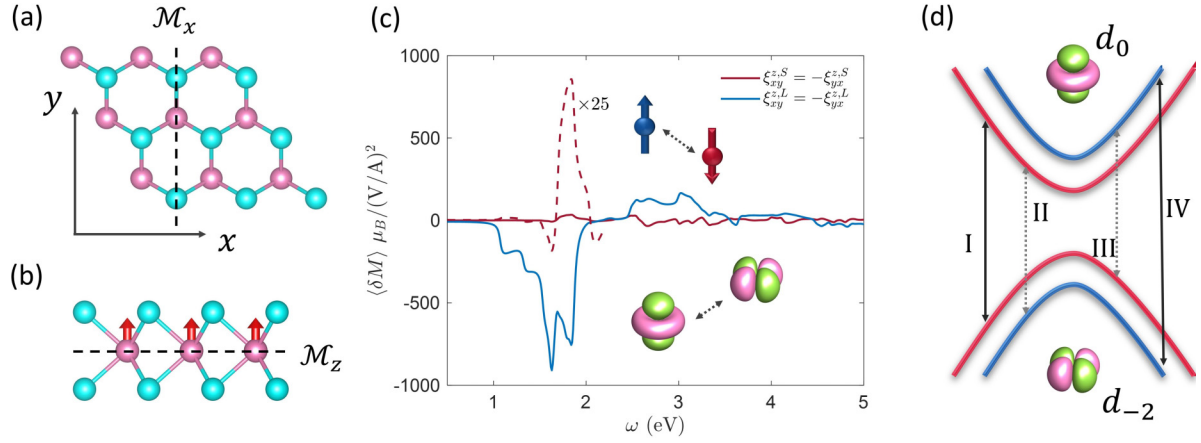


FIG. 2. (a), (b) Top and side view of monolayer MoTe₂. The mirror symmetries are indicated by the dashed line. The red arrows in (b) denote the magnetization under CPL. (c) Orbital (blue) and spin (red) contributions to the total nonlinear Edelstein effect under circularly polarized light. The dash red curve is $\xi_{xy}^{z,S}$ amplified by 25 times for $\omega < 2.2$ eV. The magnetization is shown for a primitive cell. (d) Schematic spin and orbital projected band structure of MoTe₂ near the *K* point. Blue (red) indicates spin up (down) states, while the valence and conduction bands have a major contribution from d_{-2} and d_0 orbitals, respectively. I–IV denote four possible interband transitions.

Eqs. (2) and (3) as (see Supplemental Material [25])

$$\begin{aligned} \xi_{ab}^{i,\beta}(0; \omega, -\omega) &= \tau \frac{\pi \mu_B e^2 V_{u.c.}}{2\hbar^2} \int \frac{d\mathbf{k}}{(2\pi)^3} \\ &\times \sum_{m \neq l} f_{lm} [r_{lm}^a, r_{ml}^b] (\beta_{nm}^i - \beta_{ll}^i) \delta(\omega_{ml} - \omega). \end{aligned} \quad (4)$$

Here $[r_{lm}^a, r_{ml}^b] = r_{lm}^a r_{ml}^b - r_{lm}^b r_{ml}^a$ is the interband Berry curvature, while $\Delta\beta_{ml}^i = \beta_{mm}^i - \beta_{ll}^i$ is the difference between the spin/orbital polarization on band m and l . This formalism is illustrated on the right side of Fig. 1(b): Light pumps transitions between bands m and l , and the transition rate R is determined by $R \propto [r_{lm}^a, r_{ml}^b] \delta(\omega_{ml} - \omega)$. The pumping process is compensated by the relaxation from band l back to band m , which is characterized by the relaxation time τ . In steady state, the occupation number of the conduction band m is $\delta f_{m,l} \propto R\tau$. Equation (4) simply states that the magnetization induced by light is $\delta M \propto \delta f_{m,l} \Delta\beta_{ml}^i$. MoTe₂ has a direct band gap at *K*/*K'* points, and we schematically plot the band structure of MoTe₂ near the *K* valley in Fig. 2(c), while the *K'* valley can be similarly analyzed. The valence bands and conduction bands have major contributions from $d_{-2} = \frac{1}{\sqrt{2}}(d_{x^2-y^2} - id_{xy})$ and $d_0 = d_{z^2}$ orbitals of Mo atom, respectively [25]. Each of the valence and conduction bands is twofold degenerate without SOC, and the degeneracy is broken by spin-orbit coupling (SOC). The Zeeman type spin splitting (up and down along the z direction) induced by SOC is indicated by the red (spin up) and blue (spin down) color. Note that the orbital character is mostly determined by crystal field; thus SOC does not significantly change it. There are four possible interband transitions, indicated by I–IV in Fig. 2(d). II and III have sizable ΔS^z , while I and IV have $\Delta S^z \approx 0$. However, ΔS^z of II is opposite to that of III, so the contributions from II and III tend to cancel each other and one has $\xi_{xy}^{z,S} \sim \text{II} - \text{III}$. As for the orbital part, all four transitions I–IV contribute to ΔL^z , and their contributions are the same ($\Delta L^z \approx 2$ for $d_{-2} \rightarrow d_0$) and should be summed

up; thus $\xi_{xy}^{z,L} \sim \text{I} + \text{II} + \text{III} + \text{IV}$. Furthermore, since II and III flip spin, their transition rate should be much lower than that of I and IV. Therefore, in general one would have $\xi_{xy}^{z,L} \gg \xi_{xy}^{z,S}$. In fact, light directly interacts with the orbital degree of freedom of the electrons, and leads to nonzero $\xi_{xy}^{z,L}$ with the orbital texture. The interaction is then transmitted to the spin degree of freedom by SOC, which leads to a finite $\xi_{xy}^{z,S}$ [35]. Also, the spin texture in MoTe₂ is created by SOC. Thus, one should naturally expect that the orbital contribution to the magnetization should be much greater if SOC is not too strong. Actually, without SOC, the spin-rotation symmetry is conserved, and the two valence bands and conduction bands are degenerate (no spin splitting). In this case, $\xi_{xy}^{z,S}$ vanishes, whereas $\xi_{xy}^{z,L}$ persists [25].

We now briefly compare the magnitudes of NLEE and LEE. The peak value of $\xi_{xy}^{z,T}$ is on the order of $10^3 \mu_B / (\frac{V}{\text{\AA}})^2$ [Fig. 2(c)]. We have also calculated the LEE response function ζ_a^i of MoTe₂, which exists only when the electron Fermi level \mathcal{E}_F is tuned into the valence or conduction bands, so that the system becomes metallic. When \mathcal{E}_F is 0.2 eV inside the valence or conduction bands, ζ_a^i is on the order of $0.1 \sim 1 \mu_B / \frac{V}{\text{\AA}}$ [25]. This indicates that with $E \gtrsim 10$ MV/m, the NLEE strength would exceed that of LEE (indicated by $\xi E^2 > \zeta E$). Here we would like to remark that the NLEE magnetization can be detected by a pump-probe scheme: One first applies a strong pulsed laser to induce the magnetism in the system, then use a second weaker laser to detect the magnetism with magneto-optical effects, such as Faraday rotation, or Kerr rotation. Generally, the NLEE response tensor is on the order of $100 \mu_B / (\frac{V}{\text{\AA}})^2$ (except for nonmagnetic materials under linearly polarized light). Therefore, when the electric field from the light is on the order of 1 V/nm, the NLEE magnetization would be on the order of 1 μ_B per unit cell, which is magnitudewise comparable with that of common magnetic materials, and is readily detectable. An electric field of 1 V/nm corresponds to a light intensity of 1.3×10^{11} W/cm², which is an experimentally accessible intensity, especially with pulsed lasers.

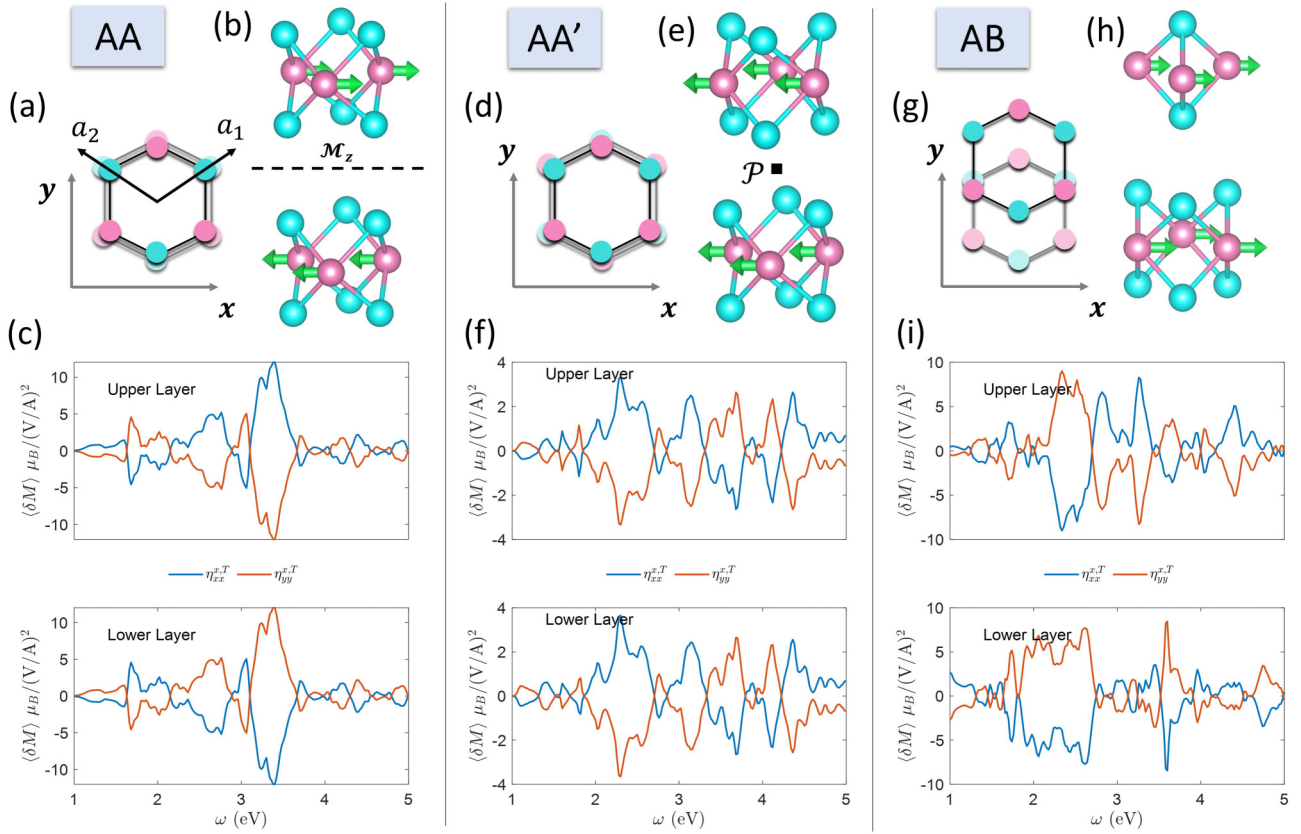


FIG. 3. The nonlinear Edelstein effect under linearly polarized light of bilayer MoTe₂ with AA (left), AA' (middle), and AB (right column) stacking patterns. (a), (d), (e) are schematic plots of the stacking pattern. (b), (e), (h) show the magnetic order under linearly polarized light with the green arrows indicate the magnetization from the nonlinear Edelstein effect. Pink: Mo; cyan: Te. (c), (f), (i) show the response function $\eta_{xx}^{x,T} = -\eta_{yy}^{x,T}$ for the upper layer and the lower layer.

C. Bilayer MoTe₂: Stacking dependent magnetic orders.

As described in the previous section, the NLEE magnetization of monolayer MoTe₂ is the same for all unit cells, which can be considered as in-plane FM ordering. On the other hand, in multilayer or multisublattice systems, the different layers or sublattices may have different chemical/structural environments, and the local NLEE magnetizations associated with these layers (sublattices) do not have to be the same. As a result, various magnetization orderings, including AFM and FM, can be realized.

Here we use bilayer MoTe₂ as an example. Two monolayer MoTe₂ are stacked along the z direction, and there can be many different stacking patterns. Three high symmetry stacking patterns of bilayer MoTe₂ are shown in Fig. 3. In AA stacking [Fig. 3(a)], Mo (Te) atoms of the upper layer sit directly above the Mo (Te) atoms of the lower layer, and the two layers are mirror images of each other, with a horizontal mirror plane \mathcal{M}_z [dashed line in Fig. 3(a)]. In AA' stacking [Fig. 3(d)], Mo (Te) atoms in the upper layer are above the Te (Mo) atoms in the lower layer, and there is an interlayer inversion symmetry \mathcal{P} ; the inversion center is indicated by the black box in Fig. 3(d). Finally, the AB stacking [Fig. 3(g)] can be obtained by shifting the upper layer of the AA stacking by a vector of $\frac{1}{3}(a_1 + a_2)$, where a_1 and a_2 are lattice vectors [Fig. 3(a)]. Note that AB stack-

ing has neither \mathcal{M}_z nor \mathcal{P} . According to our first-principles calculations, the AA' configuration has the lowest energy, and AB has slightly higher energy (0.018 eV per unit cell), whereas AA has much higher energy (0.163 eV per unit cell).

Although the van der Waals interaction between the two MoTe₂ layers is weak, the stacking pattern strongly affects the NLEE magnetization pattern. Here we calculate the layer-resolved (see Methods) response function $\eta_{xx}^{x,T} = -\eta_{yy}^{x,T}$ for all three stacking patterns. In Fig. 3, η for the upper (lower) layer corresponds to the NLEE magnetization of the upper (lower) layer under light. One can see that the NLEE magnetization patterns are distinct for the three stacking patterns: For AA stacking, η^T on the upper and lower layers are exactly opposite [Fig. 3(c)]; thus under light illumination, the NLEE magnetization on the upper and lower layers would be antiparallel, which is AFM ordering. Note that the total magnetization of the upper and lower layers is exactly zero, but the local magnetization on each layer does exist, reminiscent of the AFM order. For AA' stacking, the two layers exhibit parallel magnetization [η^T on the upper and lower layers are equal, Fig. 3(f)], which can be considered as an FM ordering. Finally, for the AB stacking, η^T on the upper and lower layers do not exhibit a simple relationship [Fig. 3(i)], and different NLEE magnetization on upper and lower layers (staggered

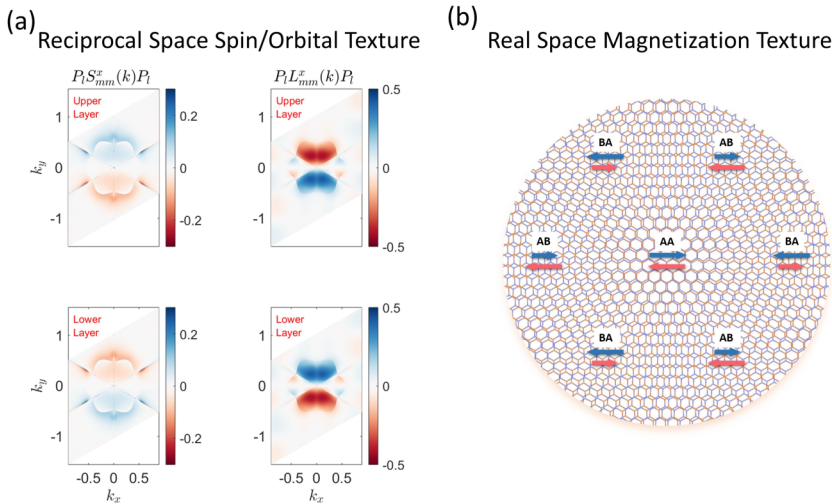


FIG. 4. (a) Reciprocal space local spin/orbital texture $P_l \beta_{mm}^x(\mathbf{k}) P_l$ for the highest valence band on the upper and lower layer of bilayer MoTe_2 . The left (right) column is the spin (orbital) texture. (b) Real-space magnetization texture on a moiré pattern. The blue and pink arrows indicate magnetization on the upper and lower layers, respectively.

magnetism) is thus expected. The magnetic orderings of different stacking patterns come from symmetry constraints. For example, in AA stacking the interlayer mirror operation \mathcal{M}_z swaps the two layers and flips M^x . Consequently, local M^x associated with the two layers must be the opposite to preserve the mirror symmetry of AA stacking. Actually, this effect is also manifested in the layer-projected \mathbf{k} -space spin/orbital texture $P_l \beta_{mm}^x(\mathbf{k}) P_l$ (see Methods), as shown in Fig. 4(a) for the highest valence band. One can see that for any \mathbf{k} point, the textures on the upper and lower layers are exactly opposite to each other. In equilibrium states, the spin/orbital polarizations of all occupied states sum up to zero; hence local spin/orbital polarizations are *hidden* [36]. However, when the system is driven out of equilibrium, the hidden magnetization emerges, and an AFM magnetization appears. Similar reasonings apply to the AA' stacking pattern, where the inversion symmetry \mathcal{P} enforces FM ordering. As for AB stacking, there are no interlayer symmetry constraints; hence the magnetizations on the two layers are not directly correlated. Interestingly, when the two layers are twisted to form a moiré pattern, a real-space spin texture can be created. The moiré pattern has spatially varying stacking patterns, which leads to spatially varying magnetic orderings with NLEE [Fig. 4(b)]. Besides, the nonequilibrium magnetization can be either (anti-) parallel or perpendicular to the electric field, which may lead to interesting physical phenomena. Particularly, the (anti-) parallel electric and magnetic field can be regarded as a nonlinear axion coupling [37].

D. CrI_3 : AFM order manipulation

Until now, we have been discussing nonmagnetic materials, where the spontaneous magnetization M_0 is zero, and a nonequilibrium magnetization δM is generated under light. This can be considered as a nonmagnetic to magnetic transition. On the other hand, in magnetic materials, there is already finite spontaneous magnetization M_0 in equilibrium. Light illumination could induce an additional NLEE magnetization δM . This δM can be considered as an effective magnetic field H_{eff} , which exerts torques on M_0 . Previous studies based on LEE suggest that this H_{eff} can cause the precession of mag-

netic moments, and a magnetic phase transition may occur when H_{eff} is strong enough [4,38,39]. Recently, the AFM spintronics [7,40,41] has attracted great interest. Compared with FM materials, using AFM materials has several advantages, such as the insensitivity to external magnetic fields, the absence of stray fields, and the fast dynamics with terahertz frequency, etc. Manipulating the magnetic ordering of AFM materials requires that the torques on the two magnetic sublattices are opposite so that no net magnetization is induced. Obviously, this cannot be achieved with a static external magnetic field. A few approaches have been proposed to manipulate AFM ordering, such as electrical approaches based on LEE [5,12,42], and optical approaches [7] based on IFE [43].

Here we propose that NLEE can be an alternative methodology for manipulating AFM ordering. Compared with LEE, NLEE applies to semiconductors, and the choice of light frequency, polarization, and intensity could provide good flexibility. Furthermore, the ultrafast ultrastrong pulsed lasers render it possible to manipulate the AFM ordering, and even trigger AFM order switching (i.e., $M_0 \rightarrow -M_0$) on a picosecond timescale. To illustrate the NLEE in magnetic materials, we take bilayer CrI_3 as an example. The magnetic ground state of bilayer CrI_3 is AFM with the magnetization M_0 along the z direction [44]. To be specific, we assume that M_0 on the upper (lower) layer point downwards [upwards, inset of Fig. 5(a)]. The layer-resolved response functions η and ξ under this configuration are plotted in Fig. 5, where a positive (negative) value of η/ξ indicates a $\delta M = \eta E^2 / \xi E^2$ along the $+z$ ($-z$) direction. One can see the under CPL that δM on the two layers are parallel to each other, whereas under LPL they are (approximately) antiparallel. Notably, for $\omega \gtrsim 3$ eV, η on the upper (lower) layer is negative (positive), so δM is opposite to M_0 , which can be utilized to swap the magnetization and trigger an AFM order switching. The opposite NLEE magnetizations on the upper and lower layers are beneficial since it would keep the total magnetization zero, so that the system stays AFM. We estimate the effective magnetic field from $H_{\text{eff}} = \frac{\delta M J_{\text{ex}}}{(\mu_B)^2}$, where J_{ex} is the exchange energy between carrier spin and the local magnetic moment, and is estimated to be ~ 1 eV from band structures (see the Supplemental

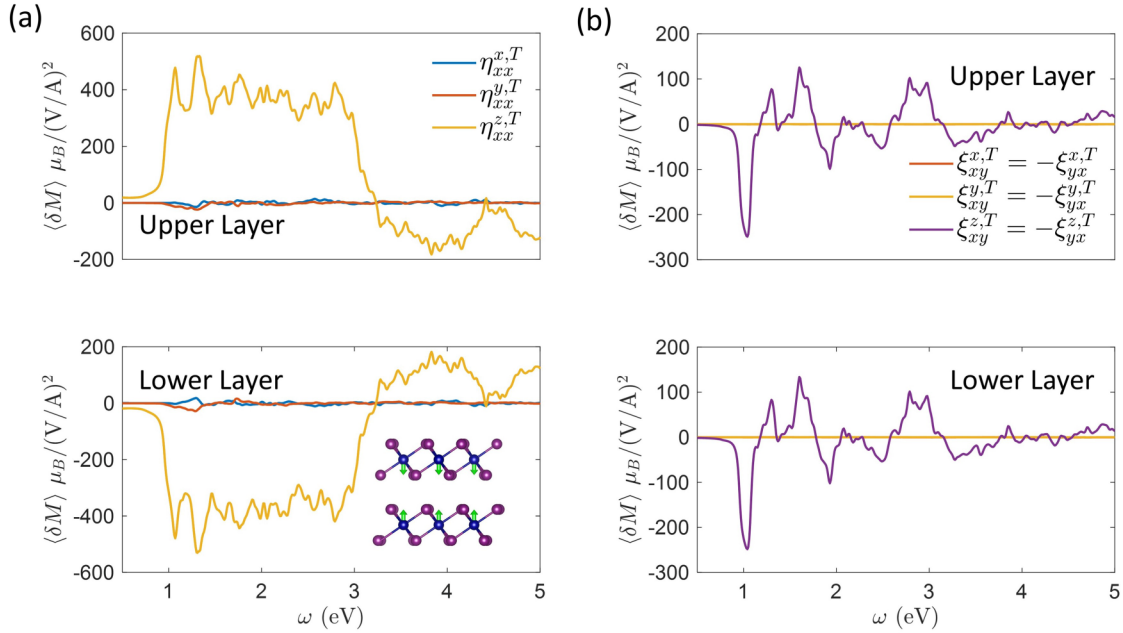


FIG. 5. Nonlinear Edelstein effect of antiferromagnetic CrI_3 with magnetization along the z axis. Under (a) linearly and (b) circularly polarized light, the light-induced magnetizations are antiparallel and parallel on the two layers, respectively. Inset of (a): atomic structure of bilayer CrI_3 . The green arrows indicate the equilibrium magnetization.

Material [25]: For an order of magnitude estimation, here we assume that carrier orbital and spin magnetization have identical exchange energy with local magnetic moment). From Fig. 5(a) one can see that η is on the order of $100 \mu_B / (\frac{V}{\text{\AA}})^2$, yielding $H_{\text{eff}} \sim 10^6 \text{ T} / (\frac{V}{\text{\AA}})^2$. Therefore, an electric field $E \sim 0.1 \text{ MV/cm}$ (corresponding to light intensity $\sim 27 \text{ MW/cm}^2$) could generate an $H_{\text{eff}} \sim 1 \text{ T}$, which is a strong enough coercive field to trigger a magnetic-order transition in CrI_3 [3]. The temperature increase under such light illumination is estimated to be on the order of 10 K [25]; thus CrI_3 can be kept below its Néel temperature, which is around 45 K [44,45].

III. DISCUSSION

First, we would like to discuss the relationship between NLEE and IFE [46–48] and ICME [49–51], which also generate an effective magnetic field H^{eff} under CPL and LPL, respectively. The light-matter interaction through the electric field can be described by the Hamiltonian $\mathcal{H}_{\text{int}} = \sum_{ab} \frac{1}{2} \varepsilon_{ab} E_a E_b^*$, where ε_{ab} is the dielectric function. Phenomenologically, IFE and ICME come from the derivative of \mathcal{H}_{int} with respect to magnetization; i.e., $H_k^{\text{eff}} = \frac{\partial \mathcal{H}_{\text{int}}}{\partial M_k} = \sum_{ab} \frac{1}{2} \frac{\partial \varepsilon_{ab}}{\partial M_k} E_a E_b^*$. The dielectric function ε_{ab} depends on the magnetic state of the system. Due to the symmetry constraints [52], to the lowest order ε satisfies $\varepsilon_{ab}^{(a)} = \sum_k \alpha_{abk} M_0^k$ and $\varepsilon_{ab}^{(s)} = \varepsilon_{ab}^0 + \frac{1}{2} \sum_{kl} \beta_{abkl} M_0^k M_0^l$, where ε^0 is vacuum permittivity, while $\varepsilon^{(a)}/\varepsilon^{(s)}$ are the asymmetric/symmetric part of ε . α_{abk} and β_{abkl} are phenomenological parameters. Thus, after the derivative with respect to M one has $H_k^{\text{IFE}} \propto \sum_{ab} \alpha_{abk} (E_a E_b^* - E_b E_a^*)$ and $H_k^{\text{ICME}} \propto \sum_{abl} \beta_{abkl} M_0^l (E_a E_b^* + E_b E_a^*)$. Consequently, in nonmagnetic materials ($M_0 = 0$), IFE can exist, while ICME must vanish. On the other hand, NLEE, which generates nonequilibrium

magnetization δM , can be understood as the derivative of \mathcal{H}_{int} with respect to magnetic field; i.e., $\delta M^k = \sum_{ab} \frac{1}{2} \frac{\partial \varepsilon_{ab}}{\partial H_k} E_a E_b^*$. Since H and M are conjugate variables, NLEE and IFE/ICME can be regarded as two complementary perspectives on the same magneto-optic effect. Notably, our quantum theory provides an approach to calculate the response function $\chi_{ab}^{i,\beta}$ with *ab initio* calculation, whereas α_{abk} and β_{abkl} are more difficult to calculate directly. In addition, we clarify that the magnetization δM , or equivalently the effective field H^{eff} , can be generated under LPL in nonmagnetic materials if the frequency of the light is above the band gap of the material, in contrast to the conclusion from the phenomenological analysis above, which suggests that H_k^{ICME} should be zero when M_0^l is zero. The reciprocity is broken by energy dissipation and the NLEE can be regarded as a nonreciprocal process.

Second, the spin dynamics in AFM materials such as CrI_3 under NLEE remains to be studied. Note that under LPL, one (approximately) has $\delta M^k \propto H_k^{\text{ICME}} \propto \sum_{abl} \beta_{abkl} M_0^l (E_a E_b^* + E_b E_a^*)$. When the magnetic anisotropy is not too strong, it is reasonable to assume that the off-diagonal terms ($k \neq l$) of β_{abkl} are much smaller the diagonal terms ($k = l$); thus H should be approximately (anti-) parallel to M_0 , which is verified by our *ab initio* calculations [25]. The spin dynamics under H with such a pattern shall be studied carefully to determine whether it is possible to trigger AFM order switching, and if possible, to determine the optimal light pulse intensity, polarization, and duration.

IV. CONCLUSION

In conclusion, we have developed a quantum theory of the nonlinear Edelstein effect, which is the generation of magnetization under light illumination. Based on symmetry analysis, we demonstrate that the NLEE is not constrained by

either spatial inversion symmetry or time-reversal symmetry, and is thus widely applicable to many materials systems in a noncontact manner. Particularly, we elucidate that orbital and spin magnetization could emerge even in conventionally nonmagnetic materials under linearly polarized light, which is counterintuitive. We attribute this to the breaking of time-reversal symmetry by the energy dissipation of photocurrents under light illumination. Then we demonstrate various features of the NLEE. First, we illustrate that the contribution from the orbital degree of freedom to the total NLEE magnetization can be much higher than that from the spin degree of freedom, which is opposite to the common notion for equilibrium (intrinsic) magnetizations. Then using bilayer MoTe₂ as an example, we show that different optomagnetic orderings, including ferromagnetic and antiferromagnetic orderings, are realizable in multilayer or multisublattice systems, depending on the symmetries that the system possesses. Finally, with bilayer CrI₃ as an example, we demonstrate that the magnetization induced by NLEE may also effectively manipulate magnetic ordering in semiconducting and insulating magnetic materials, unlike the linear Edelstein effect which is applicable only in metals. Magnitudewise, the NLEE can lead to larger magnetization than the LEE when the electric field strength is greater than 10 MV/m. Experimentally, a (pulsed) laser with electric field strength on the order of 1 V/nm would be able to generate a magnetization on the order of 1 μ_B per unit cell, which is readily detectable. The NLEE provides a convenient way to generate magnetization with light, and may find applications in, e.g., ultrafast spintronics and quantum information processing.

V. METHODS

Density functional theory and Wannier calculations

The Vienna *ab initio* simulation package (VASP) [53,54] is used for the first-principles calculations based on density functional theory (DFT) [55,56]. The exchange-correlation interactions are treated by the generalized gradient approximation (GGA) in the form of Perdew-Burke-Ernzerhof (PBE)

[57]. Projector augmented wave (PAW) method [58] and plane-wave basis functions are used to treat the core and valence electrons, respectively. For DFT calculations, the first Brillouin zone is sampled by a Γ -centered \mathbf{k} mesh with a grid of $25 \times 25 \times 1$ for MoTe₂ and $15 \times 15 \times 1$ for CrI₃. The DFT+ U method is adopted to treat the d orbitals of spin polarized Cr atoms in CrI₃ ($U = 3.0$ eV). Tight-binding orbitals are generated from Bloch waves in DFT calculations, using the WANNIER90 package [59]. The tight-binding Hamiltonian is then used to interpolate the band structure on a much denser \mathbf{k} mesh to calculate the LEE and NLEE response functions, which is $512 \times 512 \times 1$ for MoTe₂, and $320 \times 320 \times 1$ for CrI₃. The \mathbf{k} -mesh convergence is well tested. In order to calculate the real-space local magnetization, we define a projection operator $P_l = \sum_{i \in l} |\psi_i\rangle\langle\psi_i|$, where l denotes the spatial region (e.g., l th layer in a multilayer system, or the l th sublattice in a multisublattice system), while $|\psi_i\rangle$ is the tight-binding orbital belonging to region l . Then the operator $P_l \beta P_l$ is to replace β operator in Eq. (2). We simply used atomic orbitals (s , p , d , etc.) to calculate the orbital angular momentum ($\beta = L$), so only the contribution from the intra-atom term $\langle n\mathbf{R}|\mathbf{r} \times \mathbf{p}|m\mathbf{R}\rangle$ is included, while the contribution from the interatom term $\langle n\mathbf{R}|\mathbf{r} \times \mathbf{p}|m\mathbf{R}'\rangle$ is neglected. The model assumptions of (a) a uniform carrier lifetime τ for all electronic states, and (b) only atomic orbitals (s , p , d , etc.) $\langle n\mathbf{R}|\mathbf{r} \times \mathbf{p}|m\mathbf{R}\rangle$ contributing to the total orbital angular momentum, while neglecting interatomic $\langle n\mathbf{R}|\mathbf{r} \times \mathbf{p}|m\mathbf{R}'\rangle$ contributions, can certainly be systematically improved in future works.

The MATLAB code for calculating the NLEE magnetization is available at [60].

ACKNOWLEDGMENTS

This work was supported by an Office of Naval Research MURI through Grant No. N00014-17-1-2661. We are grateful for discussions with Zhurun Ji and Hanyu Zhu.

-
- [1] I. Žutić, J. Fabian, and S. Das Sarma, Spintronics: Fundamentals and applications, *Rev. Mod. Phys.* **76**, 323 (2004).
- [2] S. D. Bader and S. S. P. Parkin, Spintronics, *Annu. Rev. Condens. Matter Phys.* **1**, 71 (2010).
- [3] B. Huang, G. Clark, D. R. Klein, D. MacNeill, E. Navarro-Moratalla, K. L. Seyler, N. Wilson, M. A. McGuire, D. H. Cobden, D. Xiao, W. Yao, P. Jarillo-Herrero, and X. Xu, Electrical control of 2D magnetism in bilayer CrI₃, *Nat. Nanotechnol.* **13**, 544 (2018).
- [4] A. Kirilyuk, A. V. Kimel, and T. Rasing, Ultrafast optical manipulation of magnetic order, *Rev. Mod. Phys.* **82**, 2731 (2010).
- [5] J. Železný, H. Gao, K. Výborný, J. Zemen, J. Mašek, A. Manchon, J. Wunderlich, J. Sinova, and T. Jungwirth, Relativistic Néel-Order Fields Induced by Electrical Current in Antiferromagnets, *Phys. Rev. Lett.* **113**, 157201 (2014).
- [6] P. Wadley, B. Howells, J. Železný, C. Andrews, V. Hills, R. P. Campion, V. Novák, K. Olejník, F. Maccherozzi, S. S. Dhesi, S. Y. Martin, T. Wagner, J. Wunderlich, F. Freimuth, Y. Mokrousov, J. Kuneš, J. S. Chauhan, M. J. Grzybowski, A. W. Rushforth, K. Edmond *et al.*, Spintronics: Electrical switching of an antiferromagnet, *Science* **351**, 587 (2016).
- [7] P. Němec, M. Fiebig, T. Kampfrath, and A. V. Kimel, Antiferromagnetic opto-spintronics, *Nat. Phys.* **14**, 229 (2018).
- [8] V. M. Edelstein, Spin polarization of conduction electrons induced by electric current in two-dimensional asymmetric electron systems, *Solid State Commun.* **73**, 233 (1990).
- [9] J. C. R. Sánchez, L. Vila, G. Desfonds, S. Gambarelli, J. P. Attané, J. M. De Teresa, C. Magén, and A. Fert, Spin-to-charge conversion using Rashba coupling at the interface between nonmagnetic materials, *Nat. Commun.* **4**, 2944 (2013).
- [10] A. R. Mellnik, J. S. Lee, A. Richardella, J. L. Grab, P. J. Mintun, M. H. Fischer, A. Vaezi, A. Manchon, E. A. Kim, N. Samarth, and D. C. Ralph, Spin-transfer torque generated by a topological insulator, *Nature* **511**, 449 (2014).
- [11] K. Shen, G. Vignale, and R. Raimondi, Microscopic Theory of the Inverse Edelstein Effect, *Phys. Rev. Lett.* **112**, 096601 (2014).

- [12] L. Salemi, M. Berritta, A. K. Nandy, and P. M. Oppeneer, Orbitaly dominated Rashba-Edelstein effect in noncentrosymmetric antiferromagnets, *Nat. Commun.* **10**, 5381 (2019).
- [13] X. Li, H. Chen, and Q. Niu, Out-of-plane carrier spin in transition-metal dichalcogenides under electric current, *Proc. Natl. Acad. Sci. U. S. A.* **117**, 16749 (2020).
- [14] M. Fiebig, Revival of the magnetoelectric effect, *J. Phys. D: Appl. Phys.* **38**, 123 (2005).
- [15] S. Wienholdt, D. Hinzke, and U. Nowak, THz Switching of Antiferromagnets and Ferrimagnets, *Phys. Rev. Lett.* **108**, 247207 (2012).
- [16] A. V. Kimel, A. Kirilyuk, P. A. Usachev, R. V. Pisarev, A. M. Balbashov, and T. Rasing, Ultrafast non-thermal control of magnetization by instantaneous photomagnetic pulses, *Nature* **435**, 655 (2005).
- [17] A. M. Kalashnikova, A. V. Kimel, R. V. Pisarev, V. N. Gridnev, A. Kirilyuk, and T. Rasing, Impulsive Generation of Coherent Magnons by Linearly Polarized Light in the Easy-Plane Antiferromagnet FeBO₃, *Phys. Rev. Lett.* **99**, 167205 (2007).
- [18] R. Von Baltz and W. Kraut, Theory of the bulk photovoltaic effect in pure crystals, *Phys. Rev. B* **23**, 5590 (1981).
- [19] V. M. Fridkin, Bulk photovoltaic effect in noncentrosymmetric crystals, *Crystallogr. Rep.* **46**, 654 (2001).
- [20] S. M. Young and A. M. Rappe, First Principles Calculation of the Shift Current Photovoltaic Effect in Ferroelectrics, *Phys. Rev. Lett.* **109**, 116601 (2012).
- [21] C. L. Degen, F. Reinhard, and P. Cappellaro, Quantum sensing, *Rev. Mod. Phys.* **89**, 035002 (2017).
- [22] W. Kraut and R. Von Baltz, Anomalous bulk photovoltaic effect in ferroelectrics: A quadratic response theory, *Phys. Rev. B* **19**, 1548 (1979).
- [23] H. Xu, H. Wang, J. Zhou, and J. Li, Pure Spin photocurrent in non-centrosymmetric crystals: Bulk spin photovoltaic effect, [arXiv:2006.16945](https://arxiv.org/abs/2006.16945).
- [24] Y. Gao, C. Wang, and D. Xiao, Topological inverse Faraday effect in Weyl semimetals, [arXiv:2009.13392](https://arxiv.org/abs/2009.13392).
- [25] See Supplemental Material at <http://link.aps.org/supplemental/10.1103/PhysRevB.103.205417> for derivations of the response functions, and additional information; also see Refs. [18,22,26–33].
- [26] G. B. Ventura, D. J. Passos, J. M. B. Lopes dos Santos, J. M. V. P. Lopes, and N. M. R. Peres, Gauge covariances and nonlinear optical responses, *Phys. Rev. B* **96**, 035431 (2017).
- [27] A. Taghizadeh, F. Hipolito, and T. G. Pedersen, Linear and nonlinear optical response of crystals using length and velocity gauges: Effect of basis truncation, *Phys. Rev. B* **96**, 195413 (2017).
- [28] J. Sipe and A. Shkrebtii, Second-order optical response in semiconductors, *Phys. Rev. B* **61**, 5337 (2000).
- [29] D. Xiao, J. Shi, and Q. Niu, Berry Phase Correction to Electron Density of States in Solids, *Phys. Rev. Lett.* **95**, 137204 (2005).
- [30] T. Thonhauser, D. Ceresoli, D. Vanderbilt, and R. Resta, Orbital Magnetization in Periodic Insulators, *Phys. Rev. Lett.* **95**, 137205 (2005).
- [31] D. Ceresoli, T. Thonhauser, D. Vanderbilt, and R. Resta, Orbital magnetization in crystalline solids: Multi-band insulators, Chern insulators, and metals, *Phys. Rev. B* **74**, 024408 (2006).
- [32] J. Shi, G. Vignale, D. Xiao, and Q. Niu, Quantum Theory of Orbital Magnetization and its Generalization to Interacting Systems, *Phys. Rev. Lett.* **99**, 197202 (2007).
- [33] M. Lopez, D. Vanderbilt, T. Thonhauser, and I. Souza, Wannier-based calculation of the orbital magnetization in crystals, *Phys. Rev. B* **85**, 014435 (2012).
- [34] M. S. Dresselhaus, Solid State Physics Part III: Magnetic Properties of Solids, retrieved from <http://web.mit.edu/6.732/www/6.732-pt3.pdf>.
- [35] D. Go, D. Jo, C. Kim, and H. W. Lee, Intrinsic Spin and Orbital Hall Effects from Orbital Texture, *Phys. Rev. Lett.* **121**, 086602 (2018).
- [36] X. Zhang, Q. Liu, J. W. Luo, A. J. Freeman, and A. Zunger, Hidden spin polarization in inversion-symmetric bulk crystals, *Nat. Phys.* **10**, 387 (2014).
- [37] F. Wilczek, Two Applications of Axion Electrodynamics, *Phys. Rev. Lett.* **58**, 1799 (1987).
- [38] C. D. Stanciu, F. Hansteen, A. V. Kimel, A. Kirilyuk, A. Tsukamoto, A. Itoh, and T. Rasing, All-Optical Magnetic Recording with Circularly Polarized Light, *Phys. Rev. Lett.* **99**, 047601 (2007).
- [39] A. V. Kimel and A. K. Zvezdin, Magnetization dynamics induced by femtosecond light pulses, *Low Temp. Phys.* **41**, 682 (2015).
- [40] V. Baltz, A. Manchon, M. Tsoi, T. Moriyama, T. Ono, and Y. Tserkovnyak, Antiferromagnetic spintronics, *Rev. Mod. Phys.* **90**, 015005 (2018).
- [41] T. Jungwirth, X. Marti, P. Wadley, and J. Wunderlich, Antiferromagnetic spintronics, *Nat. Nanotechnol.* **11**, 231 (2016).
- [42] J. Železný, H. Gao, A. Manchon, F. Freimuth, Y. Mokrousov, J. Zemen, J. Mašek, J. Sinova, and T. Jungwirth, Spin-orbit torques in locally and globally noncentrosymmetric crystals: Antiferromagnets and ferromagnets, *Phys. Rev. B* **95**, 014403 (2017).
- [43] A. V. Kimel, B. A. Ivanov, R. V. Pisarev, P. A. Usachev, A. Kirilyuk, and T. Rasing, Inertia-driven spin switching in antiferromagnets, *Nat. Phys.* **5**, 727 (2009).
- [44] B. Huang, G. Clark, E. Navarro-Moratalla, D. R. Klein, R. Cheng, K. L. Seyler, D. Zhong, E. Schmidgall, M. A. McGuire, D. H. Cobden, W. Yao, D. Xiao, P. Jarillo-Herrero, and X. Xu, Layer-dependent ferromagnetism in a van der Waals crystal down to the monolayer limit, *Nature* **546**, 270 (2017).
- [45] K. L. Seyler, D. Zhong, D. R. Klein, S. Gao, X. Zhang, B. Huang, E. Navarro-Moratalla, L. Yang, D. H. Cobden, M. A. McGuire, W. Yao, D. Xiao, P. Jarillo-Herrero, and X. Xu, Ligand-field helical luminescence in a 2D ferromagnetic insulator, *Nat. Phys.* **14**, 277 (2018).
- [46] M. Battiato, G. Barbalinardo, and P. M. Oppeneer, Quantum theory of the inverse Faraday effect, *Phys. Rev. B* **89**, 014413 (2014).
- [47] D. Popova, A. Bringer, and S. Blügel, Theory of the inverse Faraday effect in view of ultrafast magnetization experiments, *Phys. Rev. B* **84**, 214421 (2011).
- [48] M. Berritta, R. Mondal, K. Carva, and P. M. Oppeneer, Ab Initio Theory of Coherent Laser-Induced Magnetization in Metals, *Phys. Rev. Lett.* **117**, 137203 (2016).
- [49] V. N. Gridnev, Phenomenological theory for coherent magnon generation through impulsive stimulated Raman scattering, *Phys. Rev. B* **77**, 094426 (2008).
- [50] A. M. Kalashnikova, A. V. Kimel, R. V. Pisarev, V. N. Gridnev, P. A. Usachev, A. Kirilyuk, and T. Rasing, Impulsive

- excitation of coherent magnons and phonons by subpicosecond laser pulses in the weak ferromagnet FeBO₃, *Phys. Rev. B* **78**, 104301 (2008).
- [51] R. Iida, T. Satoh, T. Shimura, K. Kuroda, B. A. Ivanov, Y. Tokunaga, and Y. Tokura, Spectral dependence of photoinduced spin precession in DyFeO₃, *Phys. Rev. B* **84**, 064402 (2011).
- [52] R. Kubo, Statistical mechanical theory of irreversible processes. I. General theory and simple applications to magnetic and conduction problems, *J. Phys. Soc. Jpn.* **12**, 570 (1957).
- [53] G. Kresse and J. Furthmüller, Efficiency of ab-initio total energy calculations for metals and semiconductors using a plane-wave basis set, *Comput. Mater. Sci.* **6**, 15 (1996).
- [54] G. Kresse and J. Furthmüller, Efficient iterative schemes for ab initio total-energy calculations using a plane-wave basis set, *Phys. Rev. B* **54**, 11169 (1996).
- [55] P. Hohenberg and W. Kohn, Inhomogeneous electron gas, *Phys. Rev.* **136**, B864 (1964).
- [56] W. Kohn and L. J. Sham, Self-consistent equations including exchange and correlation effects, *Phys. Rev.* **140**, A1133 (1965).
- [57] J. P. Perdew, K. Burke, and M. Ernzerhof, Generalized Gradient Approximation Made Simple, *Phys. Rev. Lett.* **77**, 3865 (1996).
- [58] P. E. Blöchl, Projector augmented-wave method, *Phys. Rev. B* **50**, 17953 (1994).
- [59] A. A. Mostofi, J. R. Yates, G. Pizzi, Y. S. Lee, I. Souza, D. Vanderbilt, and N. Marzari, An updated version of Wannier90: A tool for obtaining maximally-localised Wannier functions, *Comput. Phys. Commun.* **185**, 2309 (2014).
- [60] <http://alum.mit.edu/www/liju99/NLEE>.

Supplementary Materials
to
Light Induced Magnetization: Nonlinear Edelstein Effect

Haowei Xu¹, Jian Zhou¹, Hua Wang¹, and Ju Li^{1,2}

¹Department of Nuclear Science and Engineering, Massachusetts Institute of Technology,
Cambridge, Massachusetts 02139, USA

¹Department of Materials Science and Engineering, Massachusetts Institute of Technology,
Cambridge, Massachusetts 02139, USA

Table of Contents

1	Derivations of Response Functions of Linear and Nonlinear Edelstein Effect	2
1.1	General Response Theory	2
1.2	Linear Edelstein Effect	5
1.3	Nonlinear Edelstein Effect	7
1.4	NLEE under CPL in \mathcal{T} -conserved Systems	8
2	Supplementary Materials for Monolayer MoTe₂	9
2.1	Spin and Orbital Contributions	9
2.2	Linear Edelstein Effect of Monolayer MoTe ₂	13
2.3	Other Contributions to the Nonlinear Magnetization	13
3	Supplementary Materials for Bilayer MoTe₂	14

4 Supplementary Materials for Bilayer CrI₃	17
4.1 NLEE of Bilayer CrI ₃ with different magnetic orientations	17
4.2 Estimation of the Exchange Energy	17
4.3 Estimation of the Temperature Rise under Light Illumination	18

1 Derivations of Response Functions of Linear and Nonlinear Edelstein Effect

In this section we derive response function of the linear and nonlinear Edelstein effect (LEE and NLEE) from linear and quadratic response theory. The derivations are in a similar fashion to that in Refs. [1, 2], and largely follows the derivations in Ref. [3].

1.1 General Response Theory

The Hamiltonian of the system can be written as

$$H = H_0 + V \tag{S1}$$

where H_0 is the unperturbed Hamiltonian, while V is a perturbation. Without the interaction term V , the equilibrium density matrix should be

$$\rho_0 = \frac{1}{Z} e^{-\beta H_0} \tag{S2}$$

where $\beta = 1/k_B T$, with k_B as the Boltzmann constant and T as the temperature. Note that $[\rho_0, H_0] = 0$. The interaction V will lead to a change in density matrix $\delta\rho$. When V is weak, perturbation theory can be applied and $\delta\rho$ can be expanded in the power of V , $\delta\rho = \rho^{(1)}(V) + \rho^{(2)}(V^2) + \dots$, where $\rho^{(n)}$ is proportional to V^n and can be obtained iteratively, as we will show below.

The von Neumann equation describes the dynamics of density matrix $\rho(t)$,

$$\frac{\partial \rho}{\partial t} = -\frac{i}{\hbar} [H, \rho] - \frac{\rho - \rho_0}{\tau} \tag{S3}$$

The last term $-\frac{\rho - \rho_0}{\tau}$ is a dissipation that describes the interaction between the system and the heat bath: the system always has the tendency to return to the equilibrium state ρ_0 .

Let $\tilde{\rho}(t) = e^{\frac{t}{\tau}} e^{i\frac{H_0}{\hbar}t} \rho(t) e^{-i\frac{H_0}{\hbar}t}$, it is straightforward to verify that

$$\frac{\partial \tilde{\rho}}{\partial t} = -\frac{i}{\hbar} [\tilde{V}, \tilde{\rho}] + \frac{\rho_0}{\tau} e^{\frac{t}{\tau}} \quad (\text{S4})$$

where $\tilde{V}(t) = e^{i\frac{H_0}{\hbar}t} V(t) e^{-i\frac{H_0}{\hbar}t}$. Then the differential equation Eq. (S4) can be integrated, yielding

$$\begin{aligned} \tilde{\rho}(t) &= \tilde{\rho}(0) - \frac{i}{\hbar} \int_0^t dt' [\tilde{V}(t'), \tilde{\rho}(t')] + \frac{\rho_0}{\tau} \int_0^t dt' e^{\frac{t'}{\tau}} \\ &= \rho_0 + \rho_0 \left(e^{\frac{t}{\tau}} - 1 \right) - \frac{i}{\hbar} \int_0^t dt' [\tilde{V}(t'), \tilde{\rho}(t')] \\ &= \rho_0 e^{\frac{t}{\tau}} - \frac{i}{\hbar} \int_0^t dt' [\tilde{V}(t'), \tilde{\rho}(t')] \\ &= \rho_0 e^{\frac{t}{\tau}} - \frac{i}{\hbar} \int_0^t dt' \left[\tilde{V}(t'), \rho_0 e^{\frac{t'}{\tau}} - \frac{i}{\hbar} \int_0^{t'} dt'' [\tilde{V}(t''), \tilde{\rho}(t'')] \right] \\ &= \rho_0 e^{\frac{t}{\tau}} - \frac{i}{\hbar} \int_0^t dt' [\tilde{V}(t'), \rho_0 e^{\frac{t'}{\tau}}] - \frac{i}{\hbar} \int_0^t dt' \left[\tilde{V}(t'), -\frac{i}{\hbar} \int_0^{t'} dt'' [\tilde{V}(t''), \tilde{\rho}(t'')] \right] \\ &= \dots \end{aligned} \quad (\text{S5})$$

By iteratively putting $\tilde{\rho}(t)$ into the bracket on the rightmost of the equation above, we can obtain

$$\begin{aligned} \tilde{\rho}^{(0)}(t) &= \rho_0 e^{\frac{t}{\tau}} \\ \tilde{\rho}^{(n+1)}(t) &= -\frac{i}{\hbar} \int_0^t dt' [\tilde{V}(t'), \tilde{\rho}^{(n)}(t')] \end{aligned} \quad (\text{S6})$$

Noticing $\rho(t) = e^{-\frac{t}{\tau}} e^{-i\frac{H_0}{\hbar}t} \tilde{\rho}(t) e^{i\frac{H_0}{\hbar}t}$, we have

$$\rho^{(0)} = \rho_0 \quad (\text{S7})$$

and

$$\begin{aligned} \rho^{(n+1)}(t) &= e^{-\frac{t}{\tau}} e^{-i\frac{H_0}{\hbar}t} \tilde{\rho}^{(n+1)}(t) e^{i\frac{H_0}{\hbar}t} \\ &= -\frac{i}{\hbar} \int_0^t dt' e^{-\frac{t}{\tau}} e^{-i\frac{H_0}{\hbar}t} [\tilde{V}(t'), \tilde{\rho}^{(n)}(t')] e^{i\frac{H_0}{\hbar}t} \\ &= -\frac{i}{\hbar} \int_0^t dt' e^{-\frac{t-t'}{\tau}} e^{-i\frac{H_0}{\hbar}(t-t')} [V(t'), \rho^{(n)}(t')] e^{i\frac{H_0}{\hbar}(t-t')} \\ &= \frac{i}{\hbar} \int_0^t dt' e^{-\frac{t-t'}{\tau}} e^{-i\frac{H_0}{\hbar}t'} [V(t-t'), \rho^{(n)}(t-t')] e^{i\frac{H_0}{\hbar}t'} \end{aligned} \quad (\text{S8})$$

Next we shall go from time domain to the frequency domain by Fourier transformations. Using

$V(t-t') = \int \frac{d\omega}{2\pi} V(\omega) e^{i\omega(t-t')}$, $\rho^{(1)}$ can be calculated as

$$\begin{aligned}
\rho_{nm}^{(1)}(t) &= \langle n | \rho^{(1)}(t) | m \rangle \\
&= \frac{i}{\hbar} \int_0^t dt' \langle n | e^{-\frac{t'}{\tau}} e^{-i\frac{H_0}{\hbar}t'} [V(t-t'), \rho_0] e^{i\frac{H_0}{\hbar}t'} | m \rangle \\
&= \frac{i}{\hbar} \int \frac{d\omega}{2\pi} \langle n | [V(\omega), \rho_0] | m \rangle e^{i\omega t} \int_0^t dt \exp\left(\frac{i}{\hbar} \left[(E_m - E_n) + \frac{i\hbar}{\tau} - \hbar\omega \right] t'\right) \\
&= \frac{i}{\hbar} \int \frac{d\omega}{2\pi} V_{nm}(\omega) (f_{mm} - f_{nn}) e^{i\omega t} \frac{\exp\left(\frac{i}{\hbar} \left[(E_m - E_n) + \frac{i\hbar}{\tau} - \hbar\omega \right] t\right) - 1}{\frac{i}{\hbar} \left[(E_m - E_n) + \frac{i\hbar}{\tau} - \hbar\omega \right]} \\
&= \int \frac{d\omega}{2\pi} e^{i\omega t} \frac{f_{nm} V_{nm}(\omega)}{E_{mn} - \hbar\omega + \frac{i\hbar}{\tau}}
\end{aligned} \tag{S9}$$

Obviously, in the frequency domain one has

$$\rho_{nm}^{(1)}(\omega; \omega) = \frac{f_{nm} V_{nm}(\omega)}{E_{mn} - \hbar\omega + \frac{i\hbar}{\tau}} \tag{S10}$$

where $f_{nm} = \langle n | \rho_0 | m \rangle$ is the equilibrium distribution function, and $V_{nm} = \langle n | V | m \rangle$. Then, the second order $\rho^{(2)}$ is

$$\begin{aligned}
\rho_{nm}^{(2)}(t) &= \langle n | \rho^{(2)}(t) | m \rangle \\
&= \frac{i}{\hbar} \int \frac{d\omega'}{2\pi} e^{i\omega t} \int_0^t dt' \exp\left(\frac{i}{\hbar} \left[(E_m - E_n) + \frac{i\hbar}{\tau} - \hbar\omega' \right] t'\right) \sum_l \left(V_{nl}(\omega') \rho_{lm}^{(1)}(t-t') - \rho_{nl}^{(1)}(t-t') V_{lm}(\omega') \right) \\
&= \int \frac{d\omega}{2\pi} \int \frac{d\omega'}{2\pi} e^{i(\omega+\omega')t} \frac{1}{E_{mn} - \hbar(\omega+\omega') + \frac{i\hbar}{\tau}} \sum_l \left(\frac{f_{lm} V_{nl}(\omega') V_{lm}(\omega)}{E_{ml} - \hbar\omega + \frac{i\hbar}{\tau}} - \frac{f_{nl} V_{nl}(\omega) V_{lm}(\omega')}{E_{ln} - \hbar\omega + \frac{i\hbar}{\tau}} \right)
\end{aligned} \tag{S11}$$

We have

$$\rho_{nm}^{(2)}(\omega + \omega'; \omega, \omega') = \frac{1}{E_{mn} - \hbar(\omega + \omega') + \frac{i\hbar}{\tau}} \sum_l \left(\frac{f_{lm} V_{nl}(\omega') V_{lm}(\omega)}{E_{ml} - \hbar\omega + \frac{i\hbar}{\tau}} - \frac{f_{nl} V_{nl}(\omega) V_{lm}(\omega')}{E_{ln} - \hbar\omega + \frac{i\hbar}{\tau}} \right) \tag{S12}$$

For an arbitrary operator θ , the thermal expectation value of θ should be

$$\langle \theta \rangle = \text{Tr}(\theta \rho) \tag{S13}$$

The equilibrium value is $\langle \theta \rangle^{(0)} = \text{Tr}(\theta \rho_0)$, while the first order response is

$$\begin{aligned}
\langle \theta \rangle^{(1)}(\omega; \omega) &= \int \frac{d\mathbf{k}}{(2\pi)^3} \sum_{mn} \theta_{mn} \rho_{nm}^{(1)}(\omega; \omega) \\
&= \int \frac{d\mathbf{k}}{(2\pi)^3} \sum_{mn} \frac{f_{nm} \theta_{mn} V_{nm}(\omega)}{E_{nm} - \hbar\omega + \frac{i\hbar}{\tau}}
\end{aligned} \tag{S14}$$

Here we use the Bloch waves $|n\mathbf{k}\rangle$ as basis functions, and the explicit dependence on \mathbf{k} is omitted. The

the second order response is

$$\begin{aligned}
\langle \theta \rangle^{(2)}(\omega + \omega'; \omega, \omega') &= \int \frac{d\mathbf{k}}{(2\pi)^3} \sum_{mn} \theta_{mn} \rho_{nm}^{(2)}(\omega + \omega'; \omega, \omega) \\
&= \int \frac{d\mathbf{k}}{(2\pi)^3} \sum_{mnl} \frac{\theta_{mn}}{E_{mn} - \hbar(\omega + \omega') + \frac{i\hbar}{\tau}} \left(\frac{f_{lm} V_{nl}(\omega') V_{lm}(\omega)}{E_{ml} - \hbar\omega + \frac{i\hbar}{\tau}} - \frac{f_{nl} V_{nl}(\omega) V_{lm}(\omega')}{E_{ln} - \hbar\omega + \frac{i\hbar}{\tau}} \right) \\
&= \int \frac{d\mathbf{k}}{(2\pi)^3} \sum_{mnl} \frac{f_{lm} V_{lm}(\omega)}{E_{ml} - \hbar\omega + \frac{i\hbar}{\tau}} \left(\frac{\theta_{mn} V_{nl}(\omega')}{E_{mn} - \hbar(\omega + \omega') + \frac{i\hbar}{\tau}} - \frac{V_{mn}(\omega') \theta_{nl}}{E_{nl} - \hbar(\omega + \omega') + \frac{i\hbar}{\tau}} \right)
\end{aligned} \tag{S15}$$

The last equity can be obtained with an interchange of dummy variables as ($n \rightarrow l, l \rightarrow m, m \rightarrow n$).

1.2 Linear Edelstein Effect

In treating the light matter interaction, there are two different but equivalent approaches. One uses the so-called *length gauge*, and V is treated as

$$V = -e\mathbf{r} \cdot \mathbf{E} \tag{S16}$$

The other uses the *velocity gauge*, which we will describe in the next section. These two gauges are equivalent, as discussed in Refs. [4, 5].

For the LEE, one needs to study metallic systems with vanishing bandgap, and it is more convenient to use the length gauge. In a infinite periodic system, it is ambiguous to defined the position operator r . A standard approach is to divide r into an *interband* (e) and an *intraband* (i) part [6],

$$r = r^{(e)} + r^{(i)} \tag{S17}$$

The interband terms ($m \neq n$) are well-defined and should be

$$r_{mn}^{(e)} = (1 - \delta_{mn}) \langle mk | r | nk' \rangle = (1 - \delta_{mn}) \delta_{kk'} \frac{v_{mn}}{i\omega_{mn}} \tag{S18}$$

However, it is not straightforward to get the diagonal terms ($m = n$). Because for a infinite periodic system, the wavefunction spreads in the entire space and $\langle nk | r | nk \rangle$ should be divergent. An alternative is to use

$$r_{mn}^{(i)} = \delta_{mn} \langle mk | r | nk' \rangle = \delta_{mn} \delta_{kk'} (\xi_{nn} + i\nabla_k) \tag{S19}$$

where $\xi_{nn}(k) = \langle u_{nk} | i\nabla_k | u_{nk} \rangle$ is the Berry connection, where $|u_{nk}\rangle$ is the cell-periodic part of the wavefunction. Note that $\xi_{nn}(k)$ is well-defined and does not suffer from divergence problem. When $r^{(i)}$ is multiplied with any function g , the derivative with respect to k leads to an additional term $\nabla_k g$ after

an integration by part. It is easy to check that for any operator O which is diagonal in k , one has

$$\langle mk|[r^{(i)}, O]|nk'\rangle = i\delta_{kk'}(O)_{mn;k} \quad (\text{S20})$$

where $(O)_{mn;k}$ is the generalized derivative of O and is defined as

$$(O)_{mn;k} = \nabla_k O_{mn} - i(\xi_{mm} - \xi_{nn})O_{mn} \quad (\text{S21})$$

When we use the length gauge, the interband part can be dealt with as a normal operator. On the other hand, the intraband part contains a derivative ∇_k and needs extra care. It is better to start from the operator form in Eq. (S8), rather than the explicit matrix component form in Eqs. (S10, S12). One has

$$\begin{aligned} \rho_{nm}^{(1)}(t) &= \langle n|\rho^{(1)}(t)|m\rangle \\ &= \frac{i}{\hbar} \int_0^t dt' \langle n|e^{-\frac{t'}{\tau}} e^{-i\frac{H_0}{\hbar}t'} [V(t-t'), \rho_0] e^{i\frac{H_0}{\hbar}t'} |m\rangle \\ &= \frac{-ie\mathbf{E}(\omega)}{\hbar} \int \frac{d\omega}{2\pi} \langle n|[\mathbf{r}^{(e)}(\omega) + \mathbf{r}^{(i)}(\omega), \rho_0]|m\rangle e^{i\omega t} \int_0^t dt' \exp\left(\frac{i}{\hbar} \left[(E_m - E_n) + \frac{i\hbar}{\tau} - \hbar\omega\right] t'\right) \\ &= \frac{-ie\mathbf{E}(\omega)}{\hbar} \int \frac{d\omega}{2\pi} \langle n|[\mathbf{r}^{(e)}(\omega) + \mathbf{r}^{(i)}(\omega), \rho_0]|m\rangle e^{i\omega t} \frac{\exp\left(\frac{i}{\hbar} \left[(E_m - E_n) + \frac{i\hbar}{\tau} - \hbar\omega\right] t\right) - 1}{\frac{i}{\hbar} \left[(E_m - E_n) + \frac{i\hbar}{\tau} - \hbar\omega\right]} \\ &= -e\mathbf{E}(\omega) \int \frac{d\omega}{2\pi} e^{i\omega t} \left\{ \frac{(1 - \delta_{mn})\mathbf{r}_{nm}(\omega)(f_{mm} - f_{nn}) + i\delta_{mn}(\rho^{(0)})_{nm;k}}{E_{mn} - \hbar\omega + \frac{i\hbar}{\tau}} \right\} \\ &= -e\mathbf{E}(\omega) \int \frac{d\omega}{2\pi} e^{i\omega t} \left\{ (1 - \delta_{mn}) \frac{f_{nm}\mathbf{r}_{nm}(\omega)}{E_{mn} - \hbar\omega + \frac{i\hbar}{\tau}} + \delta_{mn} \frac{i\nabla_{\mathbf{k}}f_n}{E_{mn} - \hbar\omega + \frac{i\hbar}{\tau}} \right\} \end{aligned} \quad (\text{S22})$$

where we have

$$\begin{aligned} \rho_{mn}^{(1,e)}(\omega) &= (1 - \delta_{mn}) \frac{-e\mathbf{E}(\omega)f_{nm}\mathbf{r}_{nm}(\omega)}{E_{mn} - \hbar\omega + \frac{i\hbar}{\tau}} \\ &= (1 - \delta_{mn}) \frac{ie\mathbf{E}(\omega)\hbar f_{nm}\mathbf{v}_{nm}(\omega)}{E_{mn}(E_{mn} - \hbar\omega + \frac{i\hbar}{\tau})} \\ \rho_{mn}^{(1,i)}(\omega) &= \delta_{mn} \frac{-ie\mathbf{E}(\omega)\nabla_{\mathbf{k}}f_n}{E_{mn} - \hbar\omega + \frac{i\hbar}{\tau}} \end{aligned} \quad (\text{S23})$$

corresponding to the interband and intraband contributions, respectively. The response function for an arbitrary operator θ should be

$$\sigma_a^\theta = \frac{ie}{\hbar} \int \frac{d\mathbf{k}}{(2\pi)^3} \left\{ \sum_{m \neq n} \frac{f_{nm}\theta_{mn}v_{nm}^a}{\omega_{mn}(\omega_{mn} - \omega + i/\tau)} - \sum_n \frac{\theta_{nn}v_{nn}^a}{-\omega + i/\tau} \delta(E_n - E_F) \right\} \quad (\text{S24})$$

where we have used the zero-temperature distribution function $f_n = H(E_n - E_F)$ and

$$\begin{aligned}\frac{\partial f_n}{\partial k_a} &= \frac{\partial f_n}{\partial E_n} \frac{\partial E_n}{\partial k_a} \\ &= v_{nn}^a \delta(E_n - E_F)\end{aligned}\tag{S25}$$

with E_F as the Fermi level. Here $H(x)$ and $\delta(x)$ are the Heaviside step function and Dirac function, respectively.

For metallic systems under static field $\omega = 0$, the major contribution comes from intraband term, and one has

$$\sigma_a^\theta = -\frac{i\tau e}{\hbar} \int \frac{d\mathbf{k}}{(2\pi)^3} \sum_n \theta_{nn} v_{nn}^a \delta(E_n - E_F)\tag{S26}$$

Replacing θ with $g\mu_B\beta$, where g is the g-factor, we obtain the response function for LEE

$$\zeta_a^{i,B} = -\frac{ig\mu_B\tau e V_{\text{u.c.}}}{\hbar} \int \frac{d\mathbf{k}}{(2\pi)^3} \sum_n \beta_{nn}^i v_{nn}^a \delta(E_n - E_F)\tag{S27}$$

where we have included the volume of a unit cell $V_{\text{u.c.}}$.

1.3 Nonlinear Edelstein Effect

For NLEE, it is more convenient to use the *velocity* gauge. The light-matter interaction is included by replacing \mathbf{p} with $\mathbf{p} - e\mathbf{A}$, which is the canonical momentum. If p only appears in the kinetic energy term $\frac{p^2}{2m}$ in the Hamiltonian, then the light-matter interaction can be treated with

$$\begin{aligned}V(\omega) &= -e \sum_{i=1}^N \mathbf{v}_i \cdot \mathbf{A}(\omega) \\ &= \frac{ie}{\omega} \sum_{i=1}^N \mathbf{v}_i \cdot \mathbf{E}(\omega)\end{aligned}\tag{S28}$$

After a second quantization, we have $V_{nm}(\omega)$ in the basis of Bloch waves

$$V_{nm}(\omega) = \frac{ie}{\omega} v_{nm}^b E_b(\omega)\tag{S29}$$

Putting Eq. (S28) back into Eq. (S15), and replacing θ with $g\mu_B\beta$, one obtains the response function for NLEE,

$$\chi_{bc}^{i,\beta}(0; \omega, -\omega) = -\frac{g\mu_\beta V_{\text{u.c.}} e^2}{\hbar^2 \omega^2} \int \frac{d\mathbf{k}}{(2\pi)^3} \sum_{mnl} \frac{f_{lm} v_{lm}^b}{\omega_{ml} - \omega + \frac{i}{\tau}} \left(\frac{\beta_{mn}^i v_{nl}^c}{\omega_{mn} + \frac{i}{\tau}} - \frac{v_{mn}^c \beta_{nl}^i}{\omega_{nl} + \frac{i}{\tau}} \right)\tag{S30}$$

where we have replaced E_{mn} with $\hbar\omega_{mn}$, and included $V_{\text{u.c.}}$. Eq. (S30) is exactly the same as Eq. (2) in

the main text.

1.4 NLEE under CPL in \mathcal{T} -conserved Systems

Under CPL in \mathcal{T} -conserved Systems, the formula Eq. (S30), which involves three-band transitions, can be simplified into a two-band formalism.

First, we need to factorize the denominators of Eq. (S30) with¹

$$\begin{aligned} D_1 &= \frac{1}{\omega_{mn} + i\delta} = \frac{P}{\omega_{mn}} - i\pi\delta(\omega_{mn}) \\ D_2 &= \frac{1}{\omega_{ml} - \omega + i\delta} = \frac{P}{\omega_{ml} - \omega} - i\pi\delta(\omega_{ml} - \omega) \end{aligned} \quad (\text{S31})$$

where P stands for the Cauchy principal value in \mathbf{k} integration. As discussed in the main text, under \mathcal{T} operation, one has $\mathcal{T}\beta^i(\mathbf{k}) = -\beta^{i*}(-\mathbf{k})$ and $\mathcal{T}v^a(\mathbf{k}) = -v^{a*}(-\mathbf{k})$. Therefore the numerator of Eq. (S30), $N^{iab}(\mathbf{k}) = \beta^i(\mathbf{k})v^a(\mathbf{k})v^b(\mathbf{k})$, transforms as $\mathcal{T}N^{iab}(\mathbf{k}) = -N^{iab*}(-\mathbf{k})$. Since the denominators are invariant under \mathcal{T} , one has $\frac{N^{iab}(\mathbf{k})}{D_1(\mathbf{k})D_2(\mathbf{k})} = -\frac{N^{iab*}(-\mathbf{k})}{D_1(-\mathbf{k})D_2(-\mathbf{k})}$. Consequently, after a summation over $\pm\mathbf{k}$, only the imaginary part of $N^{iab}(\mathbf{k})$ would contribute to the final result, and thus we can ignore the real part of $N^{iab}(\mathbf{k})$ and treat it as a purely imaginary quantity.

Under CPL, E^a and E^b has a phase difference of i . Since the static spin polarization should be a real quantity, and the numerator $N^{iab}(\mathbf{k})$ can be regarded as purely imaginary, one needs to pick up the real part of the denominator $D_1(\mathbf{k})D_2(\mathbf{k})$, which is

$$\text{Re}(D_1D_2) = \frac{P}{\omega_{mn}(\omega_{ml} - \omega)} - \pi^2\delta(\omega_{mn})\delta(\omega_{ml} - \omega) \quad (\text{S32})$$

One can see that the first and second term in Eq. (S32) corresponds to $m \neq n$ and $m = n$, respectively. In case that $\tau \rightarrow 0$, the contribution from the first term is much smaller than the second term and thus we only consider the second term.

Putting $m = n$ ($n = l$) in the first (second) term of Eq. (S30), and taking the asymmetry part ($ab \leftrightarrow -ba$), one obtains the response function under CPL,

$$\xi_{ab}^{i,\beta}(0; \omega, -\omega) = \tau \frac{\pi\mu_{\text{B}}e^2V_{\text{u.c.}}}{2\hbar^2} \int \frac{d\mathbf{k}}{(2\pi)^2} \sum_{m \neq l} f_{lm} [r_{lm}^a, r_{ml}^b] (\beta_{mm}^i - \beta_{nn}^i) \delta(\omega_{ml} - \omega) \quad (\text{S33})$$

This is exactly Eq. (4) in the main text.

One can see that $\xi_{ab}^{i,B}$ is approximately proportional to the lifetime τ , which is numerically verified in Fig. S1b. Actually, for non-magnetic materials under linearly polarized light, it can be similarly shown that the NLEE response tensor is approximately independent of τ , which is numerically verified

¹Here we only study the first term in the bracket of Eq. (S30), the second term can be treated in a similar fashion.

in Fig. S1a.

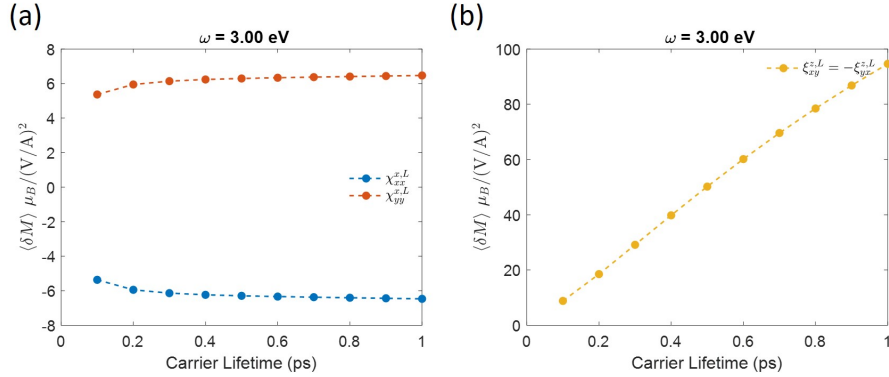


Figure S1: The NLEE response tensors as a function of carrier lifetime τ under (a) linearly polarized light and (b) circularly polarized light.

2 Supplementary Materials for Monolayer MoTe₂

2.1 Spin and Orbital Contributions

As discussed in the main text, in monolayer (ML) MoTe₂, the spin-orbit coupling (SOC) leads to Zeeman-type spin splitting. And around K -point of the Brillouin zone (BZ), the valence and conduction band (VB and CB) have major orbital contributions from d_{-2} and d_0 orbitals, respectively. These statements are supported by the spin/orbital projected band structure in Fig. S2.

The spin/orbital textures, i.e., $S_{mm}(\mathbf{k})$ and $L_{mm}(\mathbf{k})$ are plotted for the two highest VB and two lowest CB in the whole BZ, as shown in Fig. S3. One can see that the spin textures are anti-parallel for both the VBs and the CBs, while the orbital textures are parallel.

We have compared the spin texture from the tight-binding Hamiltonian and that from the plane waves of DFT, and the results are shown in Fig. S4. One can see that they agree well with each other. Note that due to the limit on the computational power, only a $64 \times 64 \times 1$ \mathbf{k} -mesh is used for the DFT calculation, so the resolution is lower in Fig. S4a.

As described in the Method section in the main text, we only used the intra-atom angular momentum matrix elements when calculating $\langle mk|L|nk\rangle$. Rigorously speaking, the inter-atomic angular momentum matrix elements should not be neglected, and in many cases their contributions are on the order of a few percent of in the total magnetization. However, the computation of these inter-atomic angular momentum matrix is rather complicated, and to the best of our knowledge, there is no standard way to do this. There is a modern theory of magnetization [7, 8, 9, 10], which can be applied

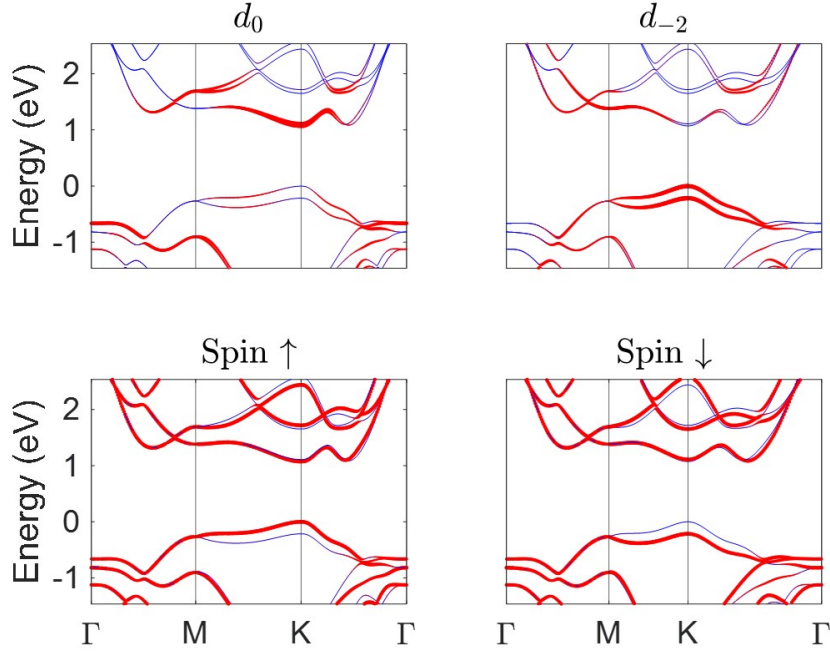


Figure S2: The projected band structure of ML MoTe₂ for d_0 and d_{-2} orbitals (upper panels), and spin up and down states (lower panels). The thin blue curves are the unprojected band structure, while the size of the red dots indicates the contribution for each spin/orbital.

to rigorously calculate the diagonal element (intraband, $m = n$) of orbital magnetization in a solid state system. We have used this modern theory of magnetization to calculate the intraband orbital texture $L_n(k) = \langle nk|L|nk\rangle$ with the WannierBerri package [<https://wannier-berri.org/>], and the results for the highest valence band are shown in Fig. S5a. The same texture calculated from the intra-atomic angular momentum (the methodology used in the current paper, omitting inter-atomic contribution) is shown in Fig. S5b. One can see that qualitatively they agree well with each other. Quantitatively, the average of the absolute value of L^z in the first Brillouin zone, $\langle L_n^z(k) \rangle = \frac{S}{(2\pi)^2} \int d^2k |L_n^z(k)|$, is $0.77 \hbar$ from modern theory of magnetization (Fig. S5a), and is $0.71 \hbar$ when only the intra-atomic angular momentum matrix elements are involved (Fig. S5b). Such a mismatch (inter-atomic contribution) on the order of 10 % is consistent with the results in e.g. Ref. [11]. In the current work, the inter-band (off-diagonal, $m \neq n$) contribution $\langle mk|L|nk\rangle$ is required, which cannot be obtained from the modern theory of magnetization. Therefore, considering computational and theoretical complexity, we use the intra-atomic orbital magnetic moment to perform our calculations.

When SOC is turned off, there are no spin-splittings, the two VB and CB will be degenerated and there are no specified spin texture. Hence the spin contribution to the total magnetization would vanish, while the orbital contribution persists. This is verified with our *ab initio* calculations, as shown in Fig. S6.

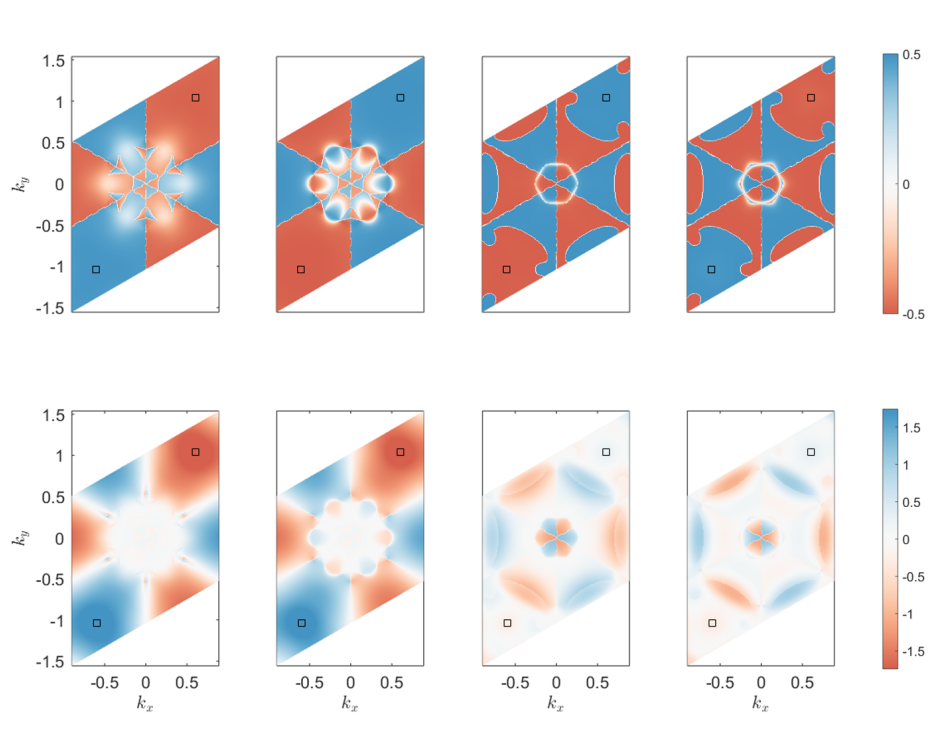


Figure S3: The spin (upper row) and orbital (lower row) textures of ML MoTe₂ for the second highest VB (first column from the left), highest VB (second column), lowest CB (third column) and second lowest CB (fourth column). The black boxes indicate K/K' points.

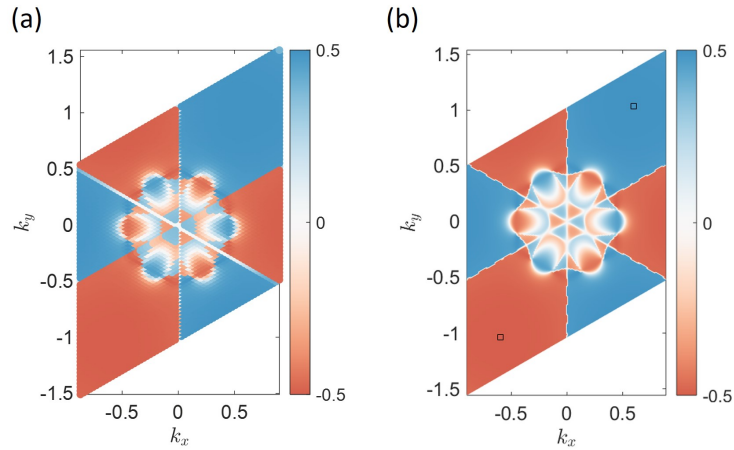


Figure S4: The spin texture of the highest valence band of monolayer MoTe₂ from (a) the plane waves of DFT and (b) tight-binding model.

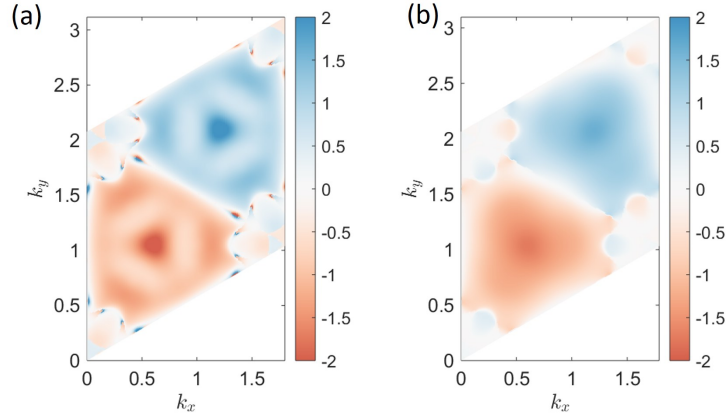


Figure S5: The orbital texture of the highest valence band of monolayer MoTe₂. (a) is calculated from the modern theory of polarization, while (b) is from the intra-atomic angular momentum matrix elements.

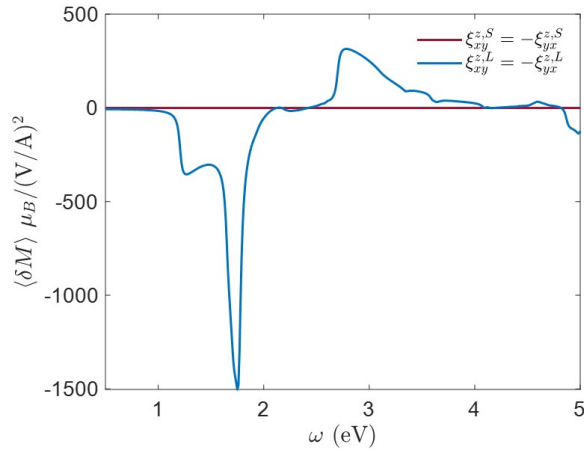


Figure S6: The NLEE response function of ML MoTe₂ without SOC. The spin contribution is zero.

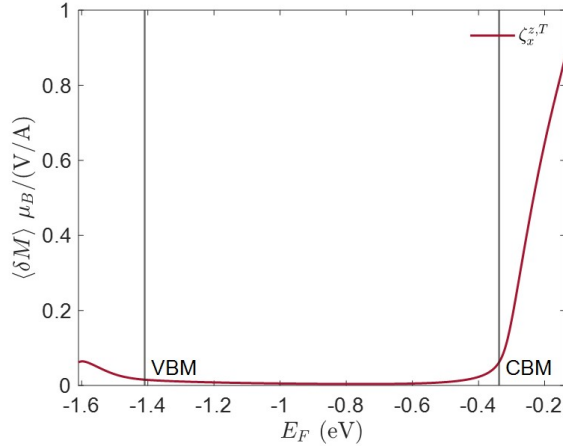


Figure S7: LEE response function ζ_a^i as a function of Fermi Level \mathcal{E}_F for ML MoTe₂. VB maximum (VBM) and CB minimum (CBM) are indicated by the two vertical lines. At $T = 0$, when \mathcal{E}_F is inside the bandgap, ζ_a^i should be zero. The finite value of ζ_a^i shown in the figure is due to a smearing factor in the numerical computation.

2.2 Linear Edelstein Effect of Monolayer MoTe₂

Since MoTe₂ is a non-magnetic semiconductor, there should be no LEE for MoTe₂ when its Fermi level \mathcal{E}_F is inside the bandgap. In order to compare the strength of NLEE and LEE, we manually vary the Fermi level, and calculate the LEE response function ζ_a^i as a function of \mathcal{E}_F , which is shown in Fig. S7. One can see that ζ_a^i is on the order of $0.1 \sim 1 \mu_B / (\frac{V}{\text{\AA}})$ when \mathcal{E}_F is 0.2 eV inside VB or CB.

2.3 Other Contributions to the Nonlinear Magnetization

Besides dipole contribution in the perturbation Eqs. (S16, S28), there could also be the quadruple interaction, and the Hamiltonian from the quadruple term is $V_{\text{quad}} = Q_{ab} \cdot \nabla_a E^b$, where Q is the quadruple of the atom and ∇E is the electric field gradient. Basically, the quadruple interaction is weaker than the dipole interaction by a factor of $\delta E / E_0$, where δE is the change in the electric field strength over a length of $\sim 1 \text{ \AA}$ (size of an atom), and E_0 is the (average) strength of the electric field. In the long wavelength limit (for optical light, the wavelength is $10^3 \sim 10^4 \text{ \AA}$), $\delta E / E_0$ is on the order of $10^{-4} \sim 10^{-3}$. For a second-order nonlinear process such as NLEE, the contribution from the quadruple interaction should be weaker than that from the dipole interaction by a factor of $(\delta E / E_0)^2 \approx 10^{-8} \sim 10^{-6}$, which is safely negligible.

The contribution from the Zeeman splitting term $V_{\text{Zeeman}} = \mu_B \mathbf{S} \cdot \mathbf{B}$ is also very weak. For a free electron moving in a plane light wave, the interaction with the magnetic field is weaker than that with the electric field by a factor of v/c , where v is the velocity of the electron and c is the velocity of light. In a solid state system, similar reasonings apply. One should expect that for NLEE, which is a second-order nonlinear effect, the contribution from $\mu_B \mathbf{S} \cdot \mathbf{B}$ is smaller than that from $e\mathbf{r} \cdot \mathbf{E}$ by

a factor of $F = (v/c)^2$, where v the band velocity in the solid system, and is usually on the order of $10^5 \sim 10^6$ m/s. Thus, one has $F \sim 10^{-7}$, and generally the contribution from the Zeeman term can be safely neglected as well. We have also directly calculated the contribution from the Zeeman term as

$$\delta M^i = \frac{g\mu_B^2 V_{u.c.}}{\hbar^2} \int \frac{d\mathbf{k}}{(2\pi)^3} \sum_{mnl} \frac{f_{lm} S_{lm}^a}{\omega_{ml} - \omega + \frac{i}{\tau}} \left(\frac{\beta_{mn}^i S_{nl}^b}{\omega_{mn} + \frac{i}{\tau}} - \frac{S_{mn}^b \beta_{nl}^i}{\omega_{nl} + \frac{i}{\tau}} \right) B^a B^b \quad (\text{S34})$$

and the result for monolayer MoTe₂ under circularly polarized light is shown in Fig. S8. Here we have converted the magnitude of magnetic field B in a plane wave to the electric field E , making use of the relationship $B = E/c$. That is, we use $\delta M^i = \chi_{ab,B}^i B^a B^b = \frac{\chi_{ab,E}^i}{c^2} E^a E^b$ and then plot $\chi_{ab,E}^i = \chi_{ab,B}^i / c^2$ in Fig. S8. Compare Fig. S8 and Figure 2c in the main text, one can observe that the contribution from the magnetic field induced Zeeman term is indeed smaller marginal by a factor of $\sim 10^{-8}$.

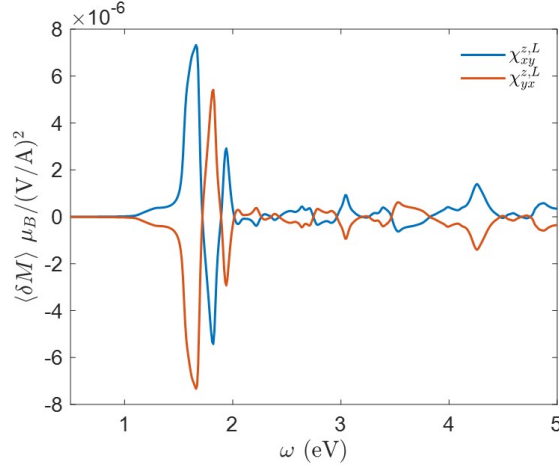


Figure S8: The nonlinear magnetization contributed from the Zeeman splitting term ($\mu_B \mathbf{S} \cdot \mathbf{B}$). The magnitude of the magnetic field has been converted to that of the electric field by $B = E/c$

3 Supplementary Materials for Bilayer MoTe₂

In the main text we show the total magnetization η^T of BL MoTe₂ under LPL. Actually, under LPL the spin and orbital parts have comparable contributions to the total magnetization. Whereas under CPL, the orbital part has much greater contribution, similar the situation in the ML MoTe₂ case. Here we take AA stacking as an example, and the results for LPL and CPL as shown in Figs. S9 and S10, respectively.

In addition, under CPL the magnetization are mostly along the z axis for all three stacking patterns AA, AA' and AB, as shown in Fig. S11.

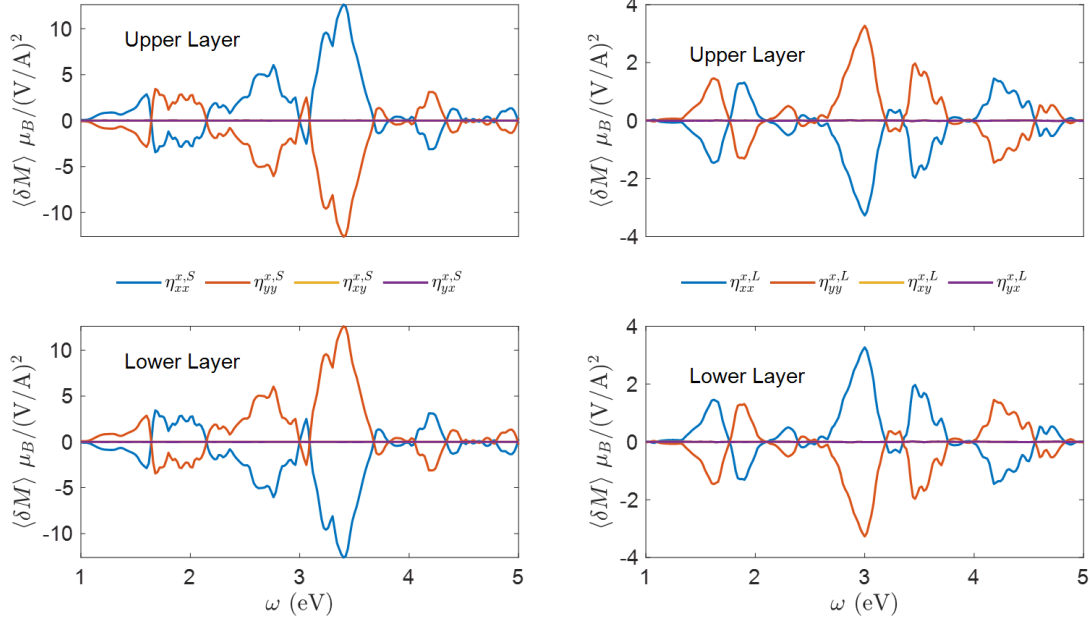


Figure S9: Spin (left column) and orbital (right column) contributions to the total magnetization of AA stacking MoTe₂ under LPL. The two contributions are comparable.

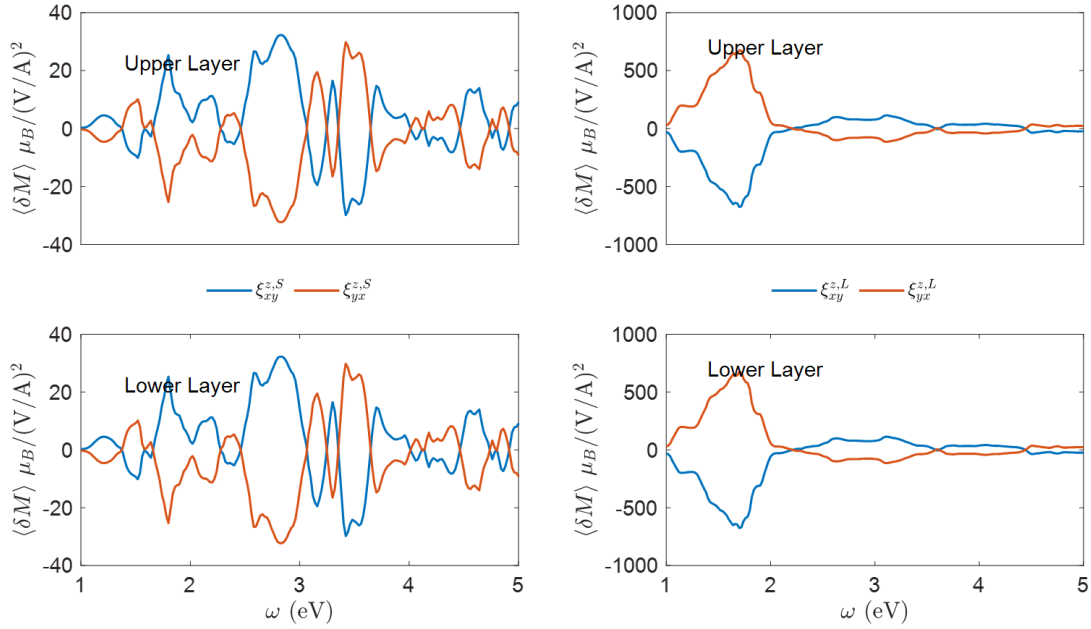


Figure S10: Spin (left column) and orbital (right column) contributions to the total magnetization of AA stacking MoTe₂ under CPL. The orbital contribution is much greater than the spin contribution.

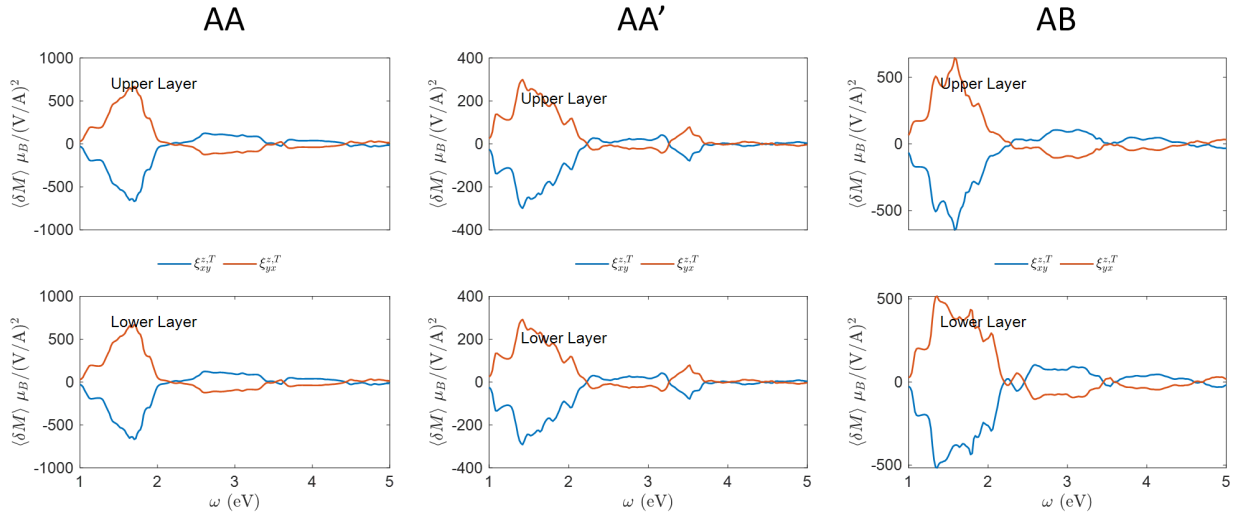


Figure S11: NLEE under CPL for AA, AA' and AB stacking patterns of BL MoTe₂. The magnetization is mostly along z axis for all three stacking patterns.

4 Supplementary Materials for Bilayer CrI₃

4.1 NLEE of Bilayer CrI₃ with different magnetic orientations

From phenomenological analysis in the main text, under LPL the NLEE magnetization should be approximately (anti-)parallel to the equilibrium magnetization. This is verified by our *ab initio* calculations with BL CrI₃. We manually fix the equilibrium magnetic moment along $x = (1, 0, 0)$, $y = (0, 1, 0)$ and $n = \frac{1}{\sqrt{3}}(1, 1, 1)$ directions, and the NLEE magnetization is found to be mostly along x , y and n , respectively, as shown in Fig. S12.

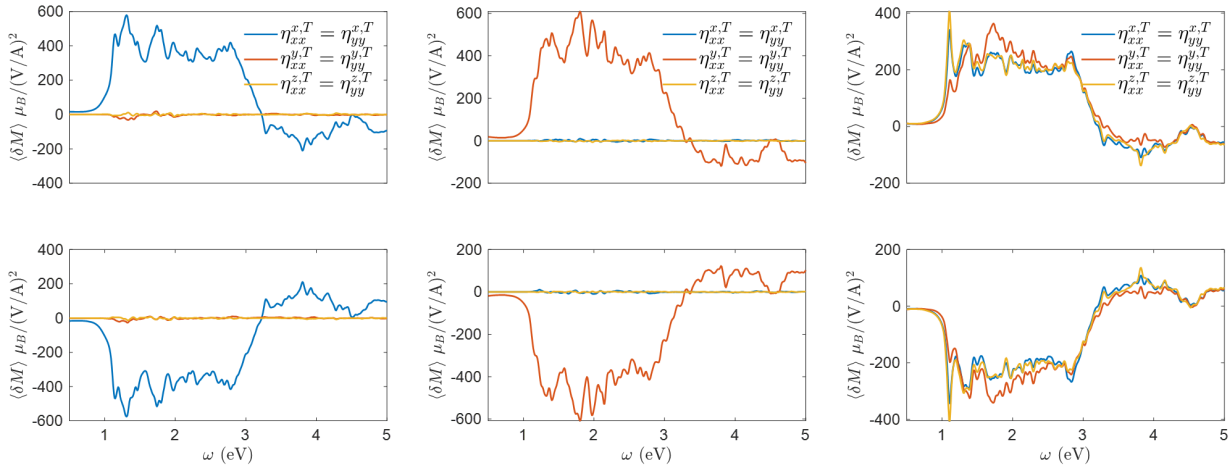


Figure S12: The NLEE magnetization under LPL of BL CrI₃ when the equilibrium magnetic moment is fixed along $x = (1, 0, 0)$ (left), $y = (0, 1, 0)$ (middle) and $n = \frac{1}{\sqrt{3}}(1, 1, 1)$ (right) directions

4.2 Estimation of the Exchange Energy

The exchange energy J_{ex} between carriers and local magnetization can be estimated from the spin splitting of energy bands of a FM system around the Fermi level. We used both FM BL CrI₃ and FM ML CrI₃, and the band structures are shown in Fig. S13. An exchange energy of $J_{\text{ex}} \sim 1$ eV is estimated.

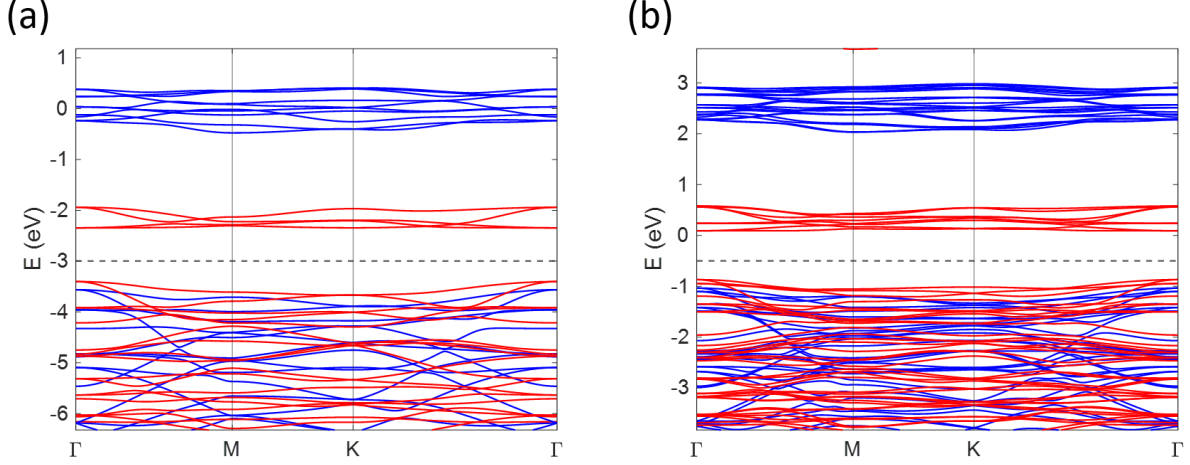


Figure S13: The band structure of (a) ML and (b) BL CrI₃ with FM ordering. SOC is not included and red and blue curves are spin up and down states. The horizontal dashed lines indicate the Fermi level. The spin splitting around the Fermi level is used to estimate the exchange energy between carriers and local magnetization.

4.3 Estimation of the Temperature Rise under Light Illumination

The energy dissipation for BL CrI₃ under light illumination can be estimated from the absorbance

$$A(\omega) = 1 - \exp\left[-\frac{\omega}{c}\varepsilon^{(2)}d\right] \quad (\text{S35})$$

where $\varepsilon^{(2)}$ is the imaginary part of the dielectric function, while d is an effective thickness. The absorbance of BL CrI₃ is shown in Fig. S14. One can see that the absorbance is roughly $A(\omega) \sim 5\%$ for $\omega > 3$ eV. Under light with intensity P , the energy absorbed by BL CrI₃ is AP . If BL CrI₃ is put on substrate with thermal conductivity κ and thickness d , then the temperature rise of BL CrI₃ can be estimated from

$$\Delta T = d \frac{AP}{\kappa} \quad (\text{S36})$$

Let $P = 27 \text{ MW/cm}^2 = 2.7 \times 10^{11} \text{ W/m}^2$, $A = 0.05$, $\kappa = 100 \text{ W} \cdot \text{m}^{-1} \cdot \text{K}^{-1}$, and $d = 100 \text{ nm}$, one can see that ΔT is only 13.5 K. Thus the temperature of BL CrI₃ can be kept below its Neel temperature with decent thermal management.

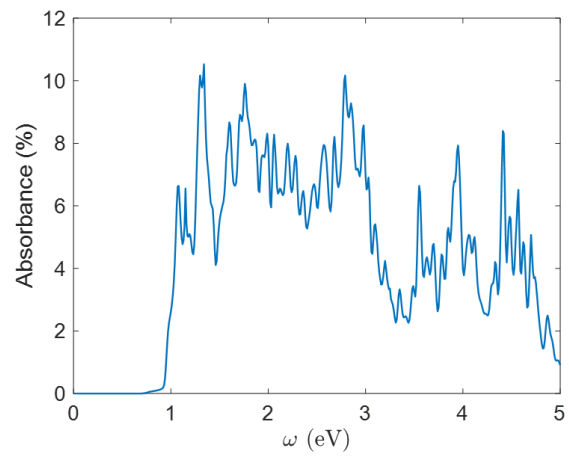


Figure S14: The absorbance of BL CrI₃.

References

- [1] Kraut, W. & von Baltz, R. Anomalous bulk photovoltaic effect in ferroelectrics: a quadratic response theory. *Physical Review B* **19**, 1548 (1979).
- [2] von Baltz, R. & Kraut, W. Theory of the bulk photovoltaic effect in pure crystals. *Physical Review B* **23**, 5590 (1981).
- [3] Xu, H., Wang, H., Zhou, J. & Li, J. Pure spin photocurrent in non-centrosymmetric crystals: Bulk spin photovoltaic effect. *arXiv preprint arXiv:2006.16945* (2020).
- [4] Ventura, G., Passos, D., dos Santos, J. L., Lopes, J. V. P. & Peres, N. Gauge covariances and nonlinear optical responses. *Physical Review B* **96**, 035431 (2017).
- [5] Taghizadeh, A., Hipólito, F. & Pedersen, T. G. Linear and nonlinear optical response of crystals using length and velocity gauges: Effect of basis truncation. *Physical Review B* **96**, 195413 (2017).
- [6] Sipe, J. & Shkrebtii, A. Second-order optical response in semiconductors. *Physical Review B* **61**, 5337 (2000).
- [7] Xiao, D., Shi, J. & Niu, Q. Berry phase correction to electron density of states in solids. *Physical review letters* **95**, 137204 (2005).
- [8] Thonhauser, T., Ceresoli, D., Vanderbilt, D. & Resta, R. Orbital magnetization in periodic insulators. *Physical review letters* **95**, 137205 (2005).
- [9] Ceresoli, D., Thonhauser, T., Vanderbilt, D. & Resta, R. Orbital magnetization in crystalline solids: Multi-band insulators, chern insulators, and metals. *Physical Review B* **74**, 024408 (2006).
- [10] Shi, J., Vignale, G., Xiao, D. & Niu, Q. Quantum theory of orbital magnetization and its generalization to interacting systems. *Physical review letters* **99**, 197202 (2007).
- [11] Lopez, M., Vanderbilt, D., Thonhauser, T. & Souza, I. Wannier-based calculation of the orbital magnetization in crystals. *Physical Review B* **85**, 014435 (2012).